NACA

RESEARCH MEMORANDUM

LOW-SPEED CASCADE TESTS OF TWO 45° SWEPT COMPRESSOR BLADES WITH CONSTANT SPANWISE LOADING

By Loren A. Beatty, Melvyn Savage, and James C. Emery

Langley Aeronautical Laboratory
Langley Field, Va.

NATIONAL ADVISORY COMMITTEE
FOR AERONAUTICS

WASHINGTON

March 15, 1954
Declassified October 14, 1957

NACA RM L53L07

NATIONAL ADVISORY COMMITTEE FOR AERONAUTICS

RESEARCH MEMORANDUM

LOW-SPEED CASCADE TESTS OF TWO 45° SWEPT COMPRESSOR BLADES WITH CONSTANT SPANWISE LOADING

By Loren A. Beatty, Melvyn Savage, and James C. Emery

SUMMARY

A cascade investigation of two 45° swept blades was conducted in the low-speed cascade tunnels at the Langley Laboratory. A series of tests was made in the 5-inch cascade tunnel at a solidity of 1.00 and an inlet-air angle of 60° on a 2.5-inch chord blade whose camber shape and twist distribution were calculated by the method of NACA TN 1350 to obtain a uniform spanwise loading. In addition, a blade of 5-inch chord, linear twist distribution, and NACA 65-($10A_2I_{8b}$)10 blade section was tested in the 10-inch cascade tunnel at inlet-air angles of 30°, 45°, and 60° at a solidity of 1.00 and at an inlet-air angle of 45° at solidities of 1.25 and 1.50. Both blades were of arrow-shaped plan form with the apex midway between the tunnel walls. Flow-visualization tests were conducted with smoke and fluorescent powder.

The twist distribution obtained from the isolated airfoil analysis in NACA TN 1350 gave an almost uniform loading over most of the blade span when tested at an inlet-air angle of 60° and solidity of 1.0. A linear twist distribution is sufficient to maintain an almost uniform loading over at least the center 50 percent of the blade semispan for inlet-air angles ranging from 0° to 60° at a solidity of 1.0 and from solidities of 1.0 to 1.5 at an inlet-air angle of 45°, over the angle-of-attack range tested. The twist distribution necessary to obtain a constant effective angle of attack and spanwise loading is practically independent of the variation in blade loading and blade loading distribution investigated herein. The angle-of-attack range of swept blades in cascade compared favorably with that of unswept blades. For the region in which uniform spanwise loading was achieved, the swept blades in cascade had streamwise blade surface pressure coefficients which, when converted to normal section pressure coefficients, were similar to those that would be obtained from the normal configuration of blade section, effective angle of attack, inlet-air angle, and solidity, tested as a cascade of unswept blades. If this result remains valid at high Mach numbers, the Mach number limit for efficient operation of the swept

blade would be approximately that of the normal section, at the normal inlet angle and solidity, divided by the cosine of the sweep angle.

INTRODUCTION

Increases in stage-pressure ratio and weight flow of multistage axial-flow compressors are necessary for the design of efficient, more powerful, light-weight turbojet engines. Increases in both weight flow and stage-pressure ratio are limited by the maximum inlet Mach numbers (relative to the blade sections) that can be used without an appreciable reduction in efficiency. The transonic rotor tests of the NACA A_2I_{8b}-series blade sections reported in reference 1 indicated that efficient operation can be maintained at transonic inlet Mach numbers. The transonic stage tests of reference 2, in which the rotor blade sections were derived to give an elliptical chordwise loading distribution and blade maximum thicknesses were kept low, also indicated efficient stage operation at transonic inlet Mach numbers.

The application of sweepback to compressor blades may permit a further increase in efficient operating Mach number level. Sweepback, however, also produces more difficult mechanical design problems such as high stress levels in rotors and increased axial depth. Although the beneficial effect of sweepback of aircraft wings is well-known, there is some question as to whether these benefits will exist in a low-aspect-ratio compressor-blade row with the confining inner and outer casings.

The use of sweep in cascade introduces a spanwise variation in induced velocity and hence induced angle of attack which does not occur in unswept cascade tests. Unpublished low-speed cascade tests conducted several years ago on an untwisted swept blade indicated that, for the cascade interference effects and high lift coefficients encountered in axial-flow compressors, the spanwise induced angles of attack due to sweep were quite pronounced. Hence, in order to obtain a constant spanwise loading distribution on a swept blade in cascade the blade must be twisted to counteract the induced spanwise angle-of-attack variation. Exact theoretical analysis of the effects of cascade variables such as inlet-air angle and solidity on such induced effects of sweep appeared to be very difficult; hence, it was decided that such cascade-induced effects would be examined by low-speed cascade tests of a blade designed by using isolated wing theory. An untapered 45° sweptback blade of arrow-shaped plan form was designed for uniform spanwise loading by using the isolated wing theory presented in reference 3 to determine the camber shape and twist distribution. In order to test a more practical configuration with a more desirable blade section, a second set of cascade blades was designed in which the theoretical twist distribution was used as a guide to determine a linear twist distribution and the NACA A_2I_{8b}-series blade section camber line described in reference 4

was used instead of the theoretically derived camber lines. The first set of blades was tested over a range of angles of attack at an inlet-air angle of 60° and a solidity of 1.0. The second set of blades was tested over a range of angles of attack at several inlet-air angles and solidities. The flow in all the tests was at a sufficiently low speed to be considered incompressible. Blade surface pressure distributions, wake measurements, and air turning angles were obtained for all blades.

In order to determine if any differences existed, the blades with the linear twist distribution were tested with two plan forms which are theoretically identical for inviscid flow. The first plan form was arrow-shaped with the apex midway between the tunnel walls. This plan form was chosen for most of the tests because it could be more easily mounted and manipulated in the cascade tunnels. The second plan form used was the half-span of the first plan form, bounded by the tunnel walls.

In addition to the tests involving the induced effects of sweep, several tests were conducted to obtain a more general understanding of swept blades in cascade. These include tests under varying wall suction conditions, a detailed static pressure survey through the blade passage, several flow-visualization tests in which smoke and fluorescent powder were used, and a series of isolated blade tests.

SYMBOLS

b	blade span
c	blade chord
C_d	drag coefficient per unit span, $D/q_1 c$
C_l	lift coefficient per unit span, $L/q_1 c$
C_{l_o}	isolated airfoil lift coefficient
C_N	normal-force coefficient per unit span, $N/q_1 c$
C_w	wake momentum difference coefficient
D	drag
g	blade gap
L	lift

M	Mach number
N	normal force
p	static pressure
P	total pressure
q	dynamic pressure
S	pressure coefficient, $\frac{P - p_1}{q_1}$
T	twist angle, $\alpha - \alpha_t$
t	blade section maximum thickness
y	coordinate
α	angle of attack
β_1	inlet-air angle
β_2	exit-air angle
Λ	sweepback angle
σ	solidity, c/g
θ	turning angle, $\beta_2 - \beta_1$

Subscripts:

1	upstream free-stream condition
2	downstream free-stream condition
av	average
c/4	25-percent-chord position
e	effective

i	induced
l	local
n	normal to the blade leading edge
t	tip

See figure 1 for cascade notation.

APPARATUS AND TEST PROCEDURE

Blade Design

The isolated wing theory of reference 3, used to obtain camber shape and twist distribution for a uniformly loaded untapered blade, replaces the arrow-shaped blade plan form by vortex sheets of constant but opposite circulation, one beginning at the blade leading edge and the other at the trailing edge and both extending to infinity. The uniform loading is assumed to exist along the entire span and the trailing vortices associated with tip loss of lift are neglected. In using this theory, a free-stream Mach number of 1.2, a sweepback angle of 45°, a chord of 2.5 inches, a span of 5 inches, and a lift coefficient of 1.0 were assumed. By using equation (20) of reference 3 the streamwise camber shape at various spanwise stations was calculated. From these camber shapes a twist distribution was obtained. (See fig. 2.) From construction considerations, the twist in the center region of the blade was faired to a value of 30°. Examination of the calculated camber shapes indicated that there was little difference in the shapes at the various spanwise stations and therefore all the calculated camber shapes were combined to form an average camber line. This average camber line, the NACA 65-010 thickness distribution applied normal to the leading edge, and the twist distribution were intended to be combined to design a swept cascade blade. A design error, however, resulted in the streamwise computed camber line being applied normal to the leading edge. Hence, the blade that was constructed and tested had the theoretical twist distribution calculated for a $C_{l_o} = 1.0$ whereas the streamwise camber line had a C_{l_o} of approximately 0.7. The theoretical twist distribution for $C_{l_o} = 0.7$ is indicated in figure 2. Over most of the blade span the error involved in using the twist associated with the blade section for C_{l_o} equal to 1.0 for a blade having a C_{l_o} equal to 0.7 is not large. In addition, the use of an isolated wing theory to determine a twist distribution for airfoils in cascade is

a considerable simplification of the problem. Hence, the twist-distribution error was not considered sufficient to justify the construction of a new set of blades. This blade is herein referred to as blade 1. (See fig. 3.)

Results of the tests on blade 1 were sufficiently satisfactory so that another arrow-shaped blade with the same sweep angle but having a more practical twist and using the NACA A_2I_{8b}-series blade mean line was designed. This 45° swept blade, hereafter referred to as blade 2A and shown in figure 4, had a chord of 5 inches and a span of 10 inches. The twist distribution that was used was linear. It was chosen to conform closely to the calculated twist used on blade 1 over most of the blade semispan and is indicated in figure 2. The streamwise section was the 65-($10A_2I_{8b}$)10 with a 1 percent trailing-edge radius. The A_2I_{8b} part of the blade designation is part of a mean line designation system which is defined in reference 4. The designation indicates that the mean line was derived by combining loadings in the following proportions for a $C_{l_o} = 1.0$: a = 1.0 for $C_{l_o} = 0.2$ and a = 0.2 backwards for $C_{l_o} = 0.8$. This mean line was selected since it exhibited good transonic performance in compressor rotor tests reported in reference 1.

In order to make a comparison of arrow-shaped and half arrow-shaped plan forms, blade 2B was constructed. This blade was a half-span model of blade 2A.

Coordinates of the streamwise sections of blades 1, 2A, and 2B are given in table 1.

Test Facilities and Procedure

The 5-inch and 10-inch cascade tunnels at the Langley Laboratory were used in this investigation. A complete description of this type of tunnel and its operation may be found in reference 5. A cross-sectional view, typical of both tunnels, is shown in figure 5.

In all tests where not stated otherwise, porous side walls were used in both tunnels along with suction slots on all four walls. Blade-setting angles were measured by a vernier inclinometer placed at the junction of the most downstream section, hereafter referred to as the tip section, and the porous wall. Because the geometrical angle of attack varied along the span and because the tip section was the most convenient measuring station, all data are referred to this angle unless otherwise specified.

Because the flow through a cascade configuration of swept blades of constant section shape is three-dimensional, a problem is presented as to the testing technique to be employed. The techniques developed in reference 5, for two-dimensional cascade testing, were to set slot suction rates to remove the wall boundary layer at the slot locations and to set the porous-wall suction rates to obtain two-dimensional flow as indicated by a comparison of the measured and calculated ratio of exit to inlet dynamic pressures. The calculated value of the exit to inlet dynamic pressure ratio was obtained by using two-dimensional-flow equations and the measured turning angle and wake width. For the tests of this investigation, the slot suction was set to remove the wall boundary layer. The initial porous-wall suction rates were set to give the ratio of the exit to inlet dynamic pressure as calculated by equations of two-dimensional flow using the measured turning angle and wake width at the center of the semispan. Tuft observations of the flow over the porous side wall and over the junction of the porous side wall and the blade were made to insure that the proper amount of flow was being removed by the porous-wall suction. Any final adjustment to the porous-wall suction rate was based on these observations.

A minimum of five blades and a maximum of seven blades were used. The number of blades used in each test was determined by the cascade configuration and the available power to give a Reynolds number of approximately 445,000 for the 5-inch chord blades and 225,000 for the $2\frac{1}{2}$-inch chord blades.

In all tests, except those of blade 1, a screen of 1/2-inch mesh hardware cloth was inserted at the entrance to the test section. This screen was inserted to increase the turbulence level of the entering air in an attempt to reduce the laminar separation encountered because power limitations necessitated operation within the critical Reynolds number range of the blade sections used.

Instrumentation for these tests consisted of several upstream wall static-pressure taps which were sufficiently far upstream to be unaffected by the blades, a multiple-tube total-pressure rake, a claw-type yaw instrument, a static-pressure surveying probe, and blade-surface static-pressure taps. The upstream wall static-pressure taps were alined parallel to the blade leading edges and were used both as an aid in determining the proper floor shape for uniform entering flow and in determining the inlet dynamic pressure. The static pressure at the cascade exit was assumed to be equal to atmospheric pressure in the calculation of exit dynamic pressure. The multiple-tube total-pressure rake was used to measure free-stream total pressure and the total-pressure loss in the blade wake. Blade turning angle was determined by the difference between the measured upstream and downstream air angles. Blade-surface static-pressure taps were located on both upper and lower blade surfaces as indicated in figure 6. These

blade surface taps were used to determine the static-pressure distribution over the blade contour at several spanwise stations. Static-pressure surveys in the blade passage were accomplished by using a long, cylindrical, static-pressure probe which could be moved through the blade passage.

Estimates of measuring accuracy are as follows:

Blade angle of attack, deg	$\pm 1/4$
Turning angles, deg	$\pm 1/2$
Static and total pressure, percent of q	$\pm 1/2$

Test Program

The cascade combinations tested for each blade are given in the following table:

β	σ		
	1.0	1.25	1.50
0°	Blade 2B	--------	--------
30°	Blade 2A	--------	--------
45°	Blade 2A Blade 2B	Blade 2A --------	Blade 2A --------
60°	Blade 1 Blade 2A	-------- --------	-------- --------

At each inlet-air angle and solidity, the angle of attack was varied over the low drag range in increments of 2° or 3°. Calculation of C_l, C_d, and L/D from the inlet-air angle, solidity, measured turning angles, and wake measurements were made by using the two-dimensional-flow equations presented in reference 6 even though two-dimensional-flow equations were not strictly applicable. The values of C_N were obtained by a mechanical integration of the local static-pressure coefficients S over the blade surface. All values of C_l, C_d, and C_N calculated were based on the upstream dynamic pressure.

Considerable variations in lift, drag, and turning angle can result from laminar separation on the blade surface: therefore, one series of tests were conducted on blade 2A over an angle-of-attack range at $\beta = 60^\circ$

and $\sigma = 1.0$ with a 1/8-inch wide strip of masking tape applied at the 35-percent-chord position on the convex and concave surfaces of each of the blades in the cascade. The purpose of these tests was to increase the local turbulence level on the blade to eliminate or greatly reduce any laminar separation that occurred.

In order to determine the effect that slot and porous side-wall suction would have on the blade characteristics, tests were made of blade 2A (the arrow-shaped blade) in which (1) suction was applied on all side walls and slots, (2) suction was applied only on the slots, and (3) no suction at all was used. These tests were made at a solidity of 1.25, an inlet-air angle of 45°, and a tip blade angle of attack of 2.8°.

Because a comparison between isolated wing and cascade configurations of the same blade was desirable, three tests were made on blade 2A at tip angles of attack of -5.4°, -2.4°, and 0.6° with all but the pressure blade removed from the cascade. No porous-wall or slot suction was used in these tests although porous side walls were used in the tunnel. These tests should give an indication of the cascade interference effects.

In order to gain an insight into the nature of the flow through the blade passage, a static-pressure survey was made with blade 2B (the half arrow-shaped blade) at $\alpha_t = 3.6^\circ$, $\beta = 45^\circ$, and $\sigma = 1.0$. This investigation included a survey of static pressure in each of three planes. The spanwise location of these planes is indicated by sections D, E, and F in figure 6. They extend from about 3 inches upstream of each leading-edge point to the location downstream at which the gapwise distribution of static pressures became constant and equal to atmospheric pressure. This survey, in conjunction with the blade surface pressures, presents a fairly complete picture of the main flow through the passage.

The flow through a blade passage was further examined by means of a series of flow-visualization tests conducted with blade 2B. The first set of these tests was conducted by using smoke to trace the flow over the blade surfaces at $\beta = 45^\circ$, $\sigma = 1.0$, and α_t ranging from -1° to 11° in 3° increments. Solid side walls were used in these tests. The smoke for these tests was produced by a small smoke generator which used as its fuel a mixture of pipe tobacco and kerosene. Air pressure of about 4 to 6 psi was sufficient to provide oxygen for burning and force enough to deliver the smoke from the generator to the blade. The smoke was then ducted into the blade and along the tubing which was cast integral with the leading-edge region of a special blade. Holes drilled into the tubing at about 3 percent of the chord downstream of the leading edge permitted the smoke to be drawn into the stream by the low blade-surface

pressure. By careful regulation of the air pressure on the smoke system, the smoke could be introduced into the flow outside of the blade surface boundary layer with a minimum of disturbance to the flow.

Another set of flow-visualization tests were conducted with a fluorescent powder. These tests were made on blade 2B at $\beta = 45^\circ$, $\sigma = 1.0$, and α_t ranging from -2.0° to 7.0°. The fluorescent powder was suspended in kerosene and then sprayed upon the surface to be investigated. Movement of air over the sprayed surface caused displacement of the powder and evaporation of the kerosene. The powder deposit could then be interpreted to indicate the nature and to some extent the direction of the boundary-layer flow. Viewing the deposit while forming and photographing of the final deposit under ultraviolet light provided the observation system for analyzing the pattern. An insight into the action of the boundary layer on the blade surface was obtained with this flow-visualization system.

RESULTS AND DISCUSSION

Results of Blade 1 Tests

Blade-surface static-pressure distributions and section characteristics are presented in figure 7 for blade 1 at a cascade combination of $\beta = 60^\circ$ and $\sigma = 1.0^\circ$ over a range of angles of attack. Figures 7(a) to 7(d) present the blade-surface static-pressure distributions for the three sections, A, B, and C, at four angles of attack. The spanwise variation of static-pressure coefficient at the 25-percent-chord location, wake coefficient, and turning angle are given in figure 7(e) and the spanwise average section characteristics are presented in figure 7(f) over the range of angles of attack tested. From figures 7(a) to 7(c), the agreement between the shape of the three pressure distributions is fairly good. Figure 7(d) indicates that section C has a lower lift coefficient as compared with sections A and B. Figure 7(e) denotes that the wake coefficient is small over most of the center portion of the blade semispan up to a tip angle of attack of 9.2°. Above $\alpha_t = 9.2^\circ$, the wake coefficient begins to rise along the span, particularly in the tip region, and indicates that this region has begun to stall. At an $\alpha_t = 12.6^\circ$, the tip stall has increased the wake coefficient appreciably over the tip 60 percent of the blade semispan. The tip stall indicated by the wake coefficients substantiates the noted loss in loading of the C section in figure 7(d). The turning-angle curves of figures 7(e) and 7(f) indicate that, although most of the blade has stalled, the increase in $d\theta/d\alpha$ with angle of attack at the root section, inferred in figure 7(e), causes the average turning angle and, therefore average C_l,

to increase with increasing angle of attack. The lift-drag ratio L/D decreased fairly rapidly because of the large increase in C_D at high angles of attack. The static-pressure coefficient of the 25-percent-chord position indicates a smooth increase in pressure from root to tip on both surfaces except at $\alpha_t = 12.6^\circ$. The sudden increase in convex surface-pressure coefficient near the root at this angle of attack may be attributed to the stall region at the blade tip.

These tests were not made over the entire low angle-of-attack region of the low drag range but are sufficient to indicate that the twist distribution applied gives reasonably uniform loading over the blade span for a fairly wide range of angle of attack. As in all cascade tests, the blade-section lift coefficient based on upstream q is considerably less than that indicated by the isolated airfoil lift coefficient of the blade section used.

Results of Blade 2A Tests

Blade-surface static-pressure distributions and section characteristics are presented over a range of angles of attack in figures 8 to 12 for blade 2A at cascade combinations of $\beta = 30^\circ$, 45°, and 60° at $\sigma = 1.0$ and $\beta = 45^\circ$ for $\sigma = 1.25$ and 1.50.

Pressure distributions.- All pressure distributions were faired to the atmospheric pressure coefficient at the 100-percent chord point. In figures 8 to 12, the pressure distributions at each spanwise station agreed very well in shape over a wide angle-of-attack range for all the combinations of inlet-air angle and solidity at which the tests were made. Similar shaped pressure distributions at each spanwise station indicate that the effective angles of attack of these sections were similar. Hence, the linear twist distribution obtained from the theoretical isolated wing calculations predicted the spanwise induced angle-of-attack distribution over at least the center 50 percent of semispan for this camber and sweep very closely for a very wide range of cascade parameters (β, σ, and α). The pressure distributions, although agreeing very well in shape, are displaced from each other in pressure-coefficient level. There is generally a gradual decrease in pressure coefficient from sections F to D along lines parallel to the leading edge. This variation in pressure coefficient at equal chord positions may be attributed to the spanwise variation in stream-tube flow area through the cascade. The effects of this spanwise variation in stream-tube flow area on the static-pressure field are discussed later in the detailed static-pressure surveys of blade 2B. Figures 8 to 12 indicate that approximately the same variation occurred for a wide range of cascade configurations and that the variation was always greatest in the trailing 50 percent of the blade. If the static pressures

the same distance ahead of each of the spanwise sections being considered were used for p_1 in calculating the pressure coefficients, instead of the upstream free-stream conditions, the pressure distributions of sections D, E, and F would more closely coincide. Hence, the C_N values of these sections would more closely coincide. Inasmuch as it would be very difficult to measure this entering static pressure along the span, all calculated values are based on the far upstream static pressure. Inasmuch as the variation in C_N with span, as indicated in figures 8 to 12, would be reduced, the linear twist distribution obtained from the theoretical isolated wing-twist calculation appears to be very effective in maintaining approximately a constant spanwise loading, C_N, over at least the center 50 percent of semispan for a wide range of cascade parameters and angles of attack.

A comparison of the tests of blades 1 and 2A seems to indicate that the required twist distribution necessary to obtain a constant effective angle of attack and loading spanwise is practically independent of the variations in blade loading and blade-loading distributions investigated herein. These results differ from those expected of isolated wings where the required twist is a function of type and magnitude of loading.

Turning angles.- Measurement of air turning angles for sweptback blades in cascade produces a problem because of the variation of the induced effects along the span. In two-dimensional-cascade testing, the turning angle is determined for a section by the difference between the downstream and upstream air angles. In the present tests, the flow is not two dimensional and, therefore, air angles measured upstream and downstream do not necessarily give a true indication of section loading. Under most conditions encountered in these tests, the upstream and downstream measuring stations were believed to be outside of the region noticeably affected by induced velocities. Measured turning angles are listed for sections D, E, and F with each pressure distribution and also plotted as a function of α_t in figures 8 to 12. The measured turning angles at sections E and D are always progressively lower than those at section F. Part of this turning-angle reduction as one progresses from F to D may be explained by noting that, because of the blade twist, the tip sections are at lower angles of attack (angles between blade chord and far upstream flow direction).

Lift, drag, and lift-drag ratio.- Discussions similar to that used in connection with C_N regarding the spanwise variation of section inlet static pressure would apply to C_l and would indicate closer C_l agreement at sections D and F. The drag coefficient cannot be reliably used for comparison between sections because it is so susceptible to local effects of Reynolds number on the blade boundary layers. From the

general trends, however, the drag coefficient is low over a large angle-of-attack range. The angle-of-attack operating range of swept blades in cascade compares favorably with that of unswept cascade blades (ref. 7). The erratic nature of the L/D curves is caused primarily by the fluctuations in the C_d curves.

Reynolds number effects.- Because these tests had to be conducted within the critical Reynolds number range of the NACA A_2I_{8b}-series blade section, considerable difficulty was encountered with laminar separation on the blade surface. A rather complete discussion of laminar separation is given in reference 7. Laminar separation, followed by reattachment of a turbulent boundary layer, is most pronounced on those pressure distributions which have a favorable pressure gradient over the forward portion of the blade. Regions of laminar separation are usually indicated by a bump in the surface pressure coefficients such as those in figures 8(a) to 8(c), 9(a) to 9(c), and 10(a) to 10(d). As a first attempt to eliminate laminar separation, these tests were conducted with a 1/2-inch square mesh hardware cloth at the entrance to the test section. As may be seen from the previously mentioned figures, this screen was not sufficient. In order to obtain one series of tests without extensive laminar separation, 1/8-inch wide strips of masking tape were applied along the 35-percent-chord positions on both the convex and concave surfaces of blade 2A. The results of the tests of this configuration at a cascade combination of $\beta = 60^\circ$ and $\sigma = 1.0$ are shown in figure 13. A comparison of the pressure distributions of figures 10 and 13 indicates that the masking tape was quite successful in removing or reducing laminar separation from both blade surfaces. However, when a very favorable gradient existed over most of the blade, as in figures 13(a) and 13(b), the surface roughness did not eliminate the laminar separation. The reduction in laminar separation effects resulted in a smooth variation in C_d and hence in L/D with angle of attack. (See figs. 10(g) and 13(g).) Although the masking tape did reduce the laminar separation effects, there was no appreciable variation in drag coefficient for the tests with and without tape. Hence, any drag reduction due to reducing laminar separation was counterbalanced by the drag added by the tape.

Comparison Between Arrow and Half Arrow Shaped Plan Form Swept Blades

In inviscid flow, an arrow-shaped blade with the apex midway between side walls is identical aerodynamically to the half-span of the same blade bounded by side walls. In order to determine the similarity between these two configurations in viscous flow, comparative tests of the half arrow blade (blade 2B) were made in the 5-inch cascade tunnel at $\beta = 45^\circ$

and $\sigma = 1.0$. Figure 14 indicates the same type of agreement between blade section data at the various spanwise locations as was obtained for the tests of the arrow-shaped blade (blade 2A). Blade 2B tests, however, indicate a reduced loading at the same tip section angle of attack. If pressure distributions of similar shape are compared (figs. 9 and 14), the blade 2B α's are some 3° higher than those of blade 2A. Figures 9 and 14 also indicate that the pressure coefficient level of blade 2B pressure distributions, at sections D, E, and F, are lower than those of blade 2A. This shift in pressure-coefficient level indicates that the pressures ahead of blade 2B must have increased over those which occur ahead of blade 2A. Hence, the effect of replacing the apex junction of the arrow-shaped blade by a porous wall to form a half arrow blade has resulted in lower pressure coefficients and a reduction in spanwise variation in angle of attack by approximately a constant 3°. No apparent explanation was found for this 3° difference in angle of attack.

Guide-Vane Tests of Blade 2B

Since half arrow shaped swept blades might be useful for some guide-vane applications, blade 2B was tested at the guide-vane condition of an inlet-air angle of 0° at a solidity of 1.0. The results are presented in figure 15. There is even better agreement between the spanwise pressure distributions for these guide-vane tests than occurred for the compressor-blade-section tests discussed in the previous sections.

Comparison of Surface Pressure Coefficients for Swept and Unswept Blades

General discussion.- The simple sweep theory of isolated wings of infinite aspect ratio indicates that the chordwise static pressure distribution over an infinite-aspect-ratio isolated wing is a function of the component of upstream velocity normal to the wing leading edge only (ref. 8). Hence, the Mach number limit for efficient operation of an infinite-aspect-ratio swept wing is limited by that of the normal airfoil section. That is, if the normal airfoil section is tested as an unswept wing and the Mach number limit for efficient operation of this unswept wing is determined, the Mach number limit for efficient operation of the swept wing will be that of the unswept wing divided by the cosine of the sweep angle. A similar phenomena would be expected from a cascade of infinite-aspect-ratio swept blades. In order to determine whether a low-aspect-ratio cascade of swept blades with confining side walls will

exhibit a similar phenomena, a comparison was made between swept and unswept blades in cascade with the same blade section and cascade parameters normal to the blade leading edge. The equations relating the normal and streamwise blade sections and cascade parameters are given in appendix A. Because of a lack of cascade data at the conditions normal to the leading edge of the swept blade, the method of reference 4 was used to estimate the pressure distribution at design angle of attack for the unswept blade. Design angle of attack is the angle of attack at which the surface velocities due to angle of attack are negligible. Measured streamwise pressure distributions on the swept blade at an angle of attack closest to the design conditions were converted to normal section pressure distributions by equation (B3).

Blades 2A and 2B.- Figure 16 presents a comparison of the converted normal pressure distribution of the E-section of swept blade 2A and the estimated pressure distribution for the unswept blade with the same blade section and cascade parameters of β and σ as existed normal to the swept blade leading edge. The streamwise cascade combinations for the swept blade tests presented in figures 16(a), 16(b), 16(c), and 16(d) are, respectively, $\beta = 30^{\circ}$, $\sigma = 1.0$; $\beta = 45^{\circ}$, $\sigma = 1.0$; $\beta = 60^{\circ}$, $\sigma = 1.0$; and $\beta = 45^{\circ}$, $\sigma = 1.5$. From figure 16 it may be seen that the agreement between converted measured and estimated pressure distributions is very good and is within the accuracy of the method of estimation of design pressure distributions, if discrepancies such as those in figures 16(a) and 16(c) due to a noticeably different effective angle of attack and to laminar separation are neglected. Hence, it appears that the converted normal pressure distributions of the E-section of swept blade 2A over the range of conditions investigated were similar to those that would be obtained if the normal configuration of blade section, β, and σ were tested as an unswept blade.

At sections D and F, the converted-measured and estimated pressure distributions agree equally well in shape; however, the static pressure coefficients obtained on these sections are, respectively, lower and higher than those of the unswept blade. Hence, it appears that, because of the confining side walls, the static pressure coefficients in the region where pressure distributions were measured (the center 50 percent of the semispan of blade 2A) decrease proceeding downstream along lines of constant chordwise position. Similar pressure-distribution-shape agreement between converted-measured and estimated pressure distributions was obtained for blade 2B, although, as indicated previously, the static pressure coefficients measured were lower than those of blade 2A.

Blade loading.- It has been established that for swept blades in cascade the blade surface static pressures are similar to those that

would be obtained if the normal configuration of blade section, β, and σ were tested as an unswept blade at least over the center 50 percent of the swept blade semispan, where the pressure distributions were measured. If the surface static pressures were identical, a swept blade with the same blade section and cascade parameters normal to the leading edge as that of an unswept blade must be operated at the same velocity normal to the leading edge as that of the unswept blade in order to obtain the same static-pressure rise.

Effect of sweepback on the Mach number limit for efficient operation.- In the region in which the agreement found between the low-speed swept normal and the unswept estimated pressure distributions remains valid at high Mach numbers, the Mach number limit for efficient operation of the swept blade will be equal to that of the normal section divided by the cosine of the sweep angle. In those regions where the swept normal pressure distribution is of the same shape as the estimated unswept pressure distribution but the static pressure coefficients are lower than those of the unswept blade, the Mach number limit for efficient operation should be slightly higher than that expected by dividing the Mach number limit for efficient operation of the unswept blade by the cosine of the sweep angle. For blade 2A, the region where this is true is from section D to E, and for blade 2B, from D to F. The Mach number limit for efficient operation will be slightly lower than that expected by dividing the Mach number limit for efficient operation of the unswept blade by the cosine of the sweep angle in the regions where the swept-blade pressure coefficients are higher. For blade 2A, the region where this is true is from E to F. For both blades there is an increase in the Mach number limit for efficient operation from sections D to E. The inlet Mach number distribution of a rotor generally increases from root to tip. Hence, the need for greater benefit of sweep with increasing radius in the rotor is in the same direction as the increased benefit due to sweep as determined in cascade. Since no data were obtained in the regions close to the confining side walls, no comments can be made as to the improvement of operating Mach number level in those regions by use of 45° sweepback.

Effects of Porous Side Walls and Slot Suction on Cascade Test Results

The results of the tests on blade 2A at $\beta = 45^\circ$, $\sigma = 1.25$, and $\alpha_t = 2.8^\circ$ with various suction conditions are shown in figure 17. Figure 17(a) presents test results in which both porous side wall and slot suction were used and is one of the tests previously presented in figure 11(d). Figure 17(b) presents test results in which there was slot suction but no porous-wall suction. In figure 17(c), there was neither porous wall nor slot suction. The porous-wall—no-suction tests do not correspond to solid-wall tests. Without suction on the porous

walls, flow may be drawn through the porous wall to the low-pressure areas on the blade surfaces. Figures 17(a) and 17(b) indicate that cutting off the porous-wall suction caused about a 1° increase in measured turning angle along the span even though the C_N value remained constant at sections E and F and decreased at section D. The pressure-distribution shapes indicate no noticeable difference in sections E and F but do indicate a very slight decrease in effective angle of attack for section D which is substantiated by the C_N values. Figure 17(c) indicates a decrease in effective angle of attack resulted when the suction was turned off. This effect was most pronounced for section D which was closest to the wall. All sections indicated a decrease in C_N associated with this decrease in angle of attack. Since suction tends to reduce wall boundary-layer growth and hence increase passage area, any reduction in suction should increase the exit pressure coefficient as indicated in figure 17. The reduction in convex-surface adverse pressure gradient associated with the reduced suction resulted in increased turning angles in figures 17(b) and 17(c) over those indicated in figure 17(a).

A comparison of figures 17(a) and 17(c) indicated that porous-wall suction has reduced the amount of convex-surface laminar separation which occurred at section F, the section farthest from the porous wall.

Figure 17(d) presents the variation of drag coefficient of sections D, E, and F for the three suction conditions. This figure indicated that the drag at the D section increased rapidly as suction was reduced whereas sections E and F were negligibly affected by suction condition.

From these tests, it may be concluded that, although slot and porous-wall suction have an effect on the magnitudes of θ, C_d, and C_N, particularly close to the wall, the twist distribution necessary to obtain a constant effective angle of attack between sections D and F appears to be negligibly affected by suction.

Isolated Wing Test of Blade 2A

Blade 2A was tested at three angles of attack with all but the pressure-distribution blade removed from the cascade to determine the cascade interference effects on a swept blade. No porous wall or slot suction was used in these tests even though porous side walls were used in the tunnel. The results of these tests are presented in figure 18. The pressure-distribution shapes of sections D, E, and F agree very well over the range of angles of attack tested. The exit pressure coefficient indicates a static-pressure rise. This is not possible for

an isolated wing; therefore, these tests are actually very low solidity tests where the two flexible floors acted as cascade blades. These tests, however, do approximate the isolated wing conditions sufficiently for the purposes of this investigation. From figures 8 to 13 and 18, it may be seen that the C_N values of the isolated blade are higher than those of the blades in cascade. As in the cascade, the C_N values increase progressively from sections D to F. Some of this variation in C_N values spanwise may be attributed to the no-suction condition with porous side walls which could permit circulation of flow from pressure to suction surface through the porous wall. Wake measurements indicate that the increase in drag coefficient of section D over sections E and F for the no-suction condition is not nearly as pronounced for the isolated case as for the case of figure 17. The fact that the pressure distributions were so similar for the isolated tests indicates that the linear twist distribution which was effective for maintaining constant spanwise effective angle of attack and loading for the cascade was also effective for the isolated wing.

Detailed Passage Static-Pressure Surveys of Blade 2B

As previously mentioned, the pressure distributions of figures 8 to 15 indicate an increasing passage inlet static pressure from midspan to wall for blade 2A and from swept forward section to wall for blade 2B. Figure 19 presents a plot of constant-static-pressure-coefficient contours through the blade passage of blade 2B at $\beta = 45^\circ$, $\sigma = 1.0$, and $\alpha_t = 3.6^\circ$. Figure 20 presents plots of static pressure coefficient against passage gap at the leading- and trailing-edge lines. These plots were obtained from detailed static-pressure surveys made through the blade passage. The spanwise static pressure gradient is evident in figures 19 and 20 by noting that the average static-pressure coefficient along the leading-edge cascade line decreases from section F to D. Figure 20 indicates that a similar type of static-pressure gradient exists along the trailing-edge cascade line. Hence, even though the pressures involved are different, the static-pressure rise through the blade passage at the F-section appears to be about the same as that through the D-section.

Flow-Visualization Studies

Previous swept-wing investigations have indicated that the component of the flow parallel to the sweep line of an infinite-aspect-ratio isolated swept wing is constant and has no effect on the blade-surface static pressures. Therefore, any changes in blade-surface static pressure will result from a variation in velocity normal to the sweep line and hence a spanwise shift of streamline curvature over the blade surface must result.

For an infinite swept blade in a cascade in which there is a static-pressure change across the blade, not only are the convex and concave surface streamlines which pass through the same leading-edge point displaced from each other spanwise at the trailing edge but, because of a lower velocity at the exit than at the inlet, they have a flow direction different from the inlet flow.

From the blade surface pressure distribution and the assumption that the component of the free-stream velocity parallel to the sweep direction remains constant over the blade surface, streamline paths over the blade surface were calculated. These paths were computed for the E section (the midspan section) at an $\alpha_t = 3.6^\circ$. (See fig. 21.) Comparisons between computed streamlines and smoke traces were made by drawing the computed streamline shapes on the airfoil and visually comparing these curves with the smoke paths during the test. Smoke introduced at the leading edge at the E section of the blade on each surface coincided with the computed paths until the smoke separated from the blade surface at about 90 to 95 percent chord for the $\alpha_t = 3.6^\circ$ test.

Figure 22 presents the results of a series of flow-visualization tests on the convex surface of blade 2B at $\beta = 45^\circ$, $\sigma = 1.0$ for $\alpha_t = -1.0^\circ$, 2.0°, 5.0°, 8.0°, and 11.0°, utilizing smoke to trace the streamline path of the flow at the outer edge of the boundary layer. This series of tests were made with solid walls in the cascade. Observation of the smoke paths at different spanwise positions indicated that the streamline paths are quite similar in shape and hence the above assumptions appear to be valid to within 1 inch from each side wall over the angles of attack investigated. Observation of smoke paths and tuft surveys indicated that the curvature of the streamlines decreased rapidly away from the blade surface. The photographs of figure 22 do not give a true indication of the variation of streamline curvature with angle of attack because a fixed camera angle was employed. Therefore, the streamline path over the convex surface of blade 2B at an $\alpha_t = 12.6^\circ$ was computed by using the pressure distribution of figure 14(f) and is compared in figure 21 to the path for a $\alpha_t = 3.6^\circ$. The variation in streamline path with angle of attack appeared to be quite small for the convex surface.

Figures 23 and 24 present the results of a series of flow-visualization tests on blade 2B at $\beta = 45^\circ$ and $\sigma = 1.0$ over a range of angles of attack in which fluorescent powder was used in a preliminary attempt to investigate boundary-layer action on swept blades in cascade. Since the suspension used in these tests is arranged by the boundary layer and the final deposition results from evaporation of the suspending liquid, regions of heavy deposit are regions of initial separation or reverse flow. Figure 23 presents photographs of the

convex surface of the blade at various angles of attack. Very close to the blade leading edge, a narrow strip of heavy powder deposit may be noted. This narrow strip is displaced in the downstream direction as angle of attack is increased. At just above $\alpha_t = 4.0^\circ$, the deposit begins to deteriorate and at approximately $\alpha_t = 7.0^\circ$ the deposit has almost completely disappeared. The action and appearance of the deposit may be the result of a small region of laminar separation. From indications of the pressure distributions presented in figure 14 and the photographs of powder deposit in figure 23, it appears that a region of laminar separation with turbulent reattachment occurs near the blade trailing edge. In order for both of these indicated conditions to occur on the same blade, the laminar separation near the blade leading edge would have to reattach as laminar boundary layer. There is some doubt as to whether this can occur even under the very favorable pressure gradient over the upstream sections of this blade. Since insufficient information is available on this subject, in the Reynolds number range of these tests (that is, approx. 445,000), definite conclusions cannot be made as to the state of the boundary layer in the leading-edge region of this blade at the conditions investigated. The turbulent regions near the root and tip are caused by blade and porous-wall interaction. As the angle of attack was increased, the trailing-edge region of presumably laminar separation decreased in extent and covered only about one-quarter of the midspan region at $\alpha_t = 7.0^\circ$. At this angle of attack, the trailing-edge laminar-separation region had moved forward. A forward shift of this laminar-separation region is substantiated in the pressure distributions of figure 14. A possible explanation for the spanwise reduction in the trailing-edge laminar-separation region with increased angle of attack is that the interaction between wall and blade becomes more pronounced at higher angles of attack. This interaction could trigger a transition from laminar to turbulent flow ahead of the region where the trailing-edge separation had occurred for lower angles of attack. Then too, the pressure gradient becomes less favorable for laminar flow as angle of attack increases and the deterioration of the phenomena at the leading edge may initiate a transition to turbulent boundary layer.

For the test at an angle of attack of 7°, an outward flow of boundary layer from the root section (the section at the apex) to the tip section was very noticeable in the trailing-edge region. Hence, under certain conditions, it might be desirable to use boundary-layer fences to keep this low energy air from piling up at the junction between the tip section and the wall.

The boundary-layer flow on the concave surface of blade 2B over a range of angles of attack is indicated in figure 24. The test at $\alpha_t = -2.0^\circ$ (fig. 24(a)) indicates that the flow over the forward portion of the concave surface is quite smooth except for about the tip

20 percent of the span. The transition to a turbulent boundary-layer flow in the tip region is probably primarily a result of a higher velocity peak near the leading edge as indicated in figure 14 and the wall-interference effects. At about 40 percent downstream of the leading edge near the root and progressively closer toward the tip the flow in a region of laminar separation abruptly turns in the spanwise direction. The striated appearance of the deposit in this region is very noticeable. The flow appears to follow this direction until about 20 percent span from the tip whereupon it appears to trail off downstream. The smooth nature of the deposit upstream of the reverse-flow region indicates that laminar flow occurs in this region. As angle of attack is increased, the laminar-separation region and the resulting spanwise flow become more pronounced and extend to the tip wall. The accumulation of the spanwise flow appears to form into a rather strong vortex near the tip wall, as indicated by a large powder deposit near the wall followed by a region which has been scrubbed clean. The amount of spanwise flow and therefore the strength of the tip vortex increased with increasing angle of attack.

General Comments Regarding Sweep

Since the benefit of sweepback in raising the operating Mach number level for the isolated infinite-aspect-ratio yawed wing is so widely known, a short discussion indicating the differences between it and a cascade of infinite-aspect-ratio yawed blades is included to aid in the application of the results of this investigation.

In the simple sweep theory of an infinite-aspect-ratio isolated yawed wing at an angle of attack of 0°, the distribution of static pressure coefficient at the section normal to the leading edge, based on the component of velocity normal to the leading edge, is independent of sweep-angle variation produced by yawing the wing. Under the same basic assumptions, for a cascade of infinite-aspect-ratio yawed blades, the static pressure coefficients over the normal section, based on the component of velocity normal to the leading edge, do vary with sweep angle. This variation in distribution and magnitude of static pressure coefficients in the case of the cascade is caused by a change in normal inlet-air angle and solidity as sweep angle changes. (The relationships between the normal and streamwise inlet-air angles and solidities are given in appendix A.) Hence, the normal Mach number limit for efficient operation of a cascade of infinite-aspect-ratio swept blades at an angle of attack of 0° varies with sweep angle. This is unlike the case of the isolated wing where, at an angle of attack of 0°, the normal Mach number limit for efficient operation is independent of sweep angle.

Although this discussion has dealt with the infinite-aspect-ratio condition, the results obtained should also apply in any region where it is found that the surface static pressures are a function of the

component of velocity normal to the leading edge. It has been indicated that the Mach number limit for efficient operation of the normal section of a cascade of swept blades will vary with sweep angle as the cascade is yawed. Therefore, the increase in limiting Mach number expected by yawing a given set of cascade blades must be compared with the variation in the normal blade section Mach number limit for efficient operation that occurs. In this way, the actual net gain in limiting Mach number obtained by varying sweepback through yaw may be determined. Although this discussion deals with a fixed configuration streamwise and obtains the sweepback through yaw, it does not preclude that, in application of sweepback to compressor blades, the normal configuration may be varied to obtain the optimum results for the particular design conditions.

The application of sweepback to compressor blades will present problems which are not now as important in the design of unswept blades. These problems will include the determination of induced angles of attack for varying loadings and blade configurations, a more severe boundary-layer problem because of the component of flow parallel to the blade leading edge, and a more difficult structural design problem in the case of swept rotor blades.

CONCLUSIONS

A cascade investigation of two 45° swept blades over a range of angles of attack at various combinations of inlet-air angle and solidity from 0° to 60° and 1.0 to 1.5, respectively, indicated the following conclusions:

1. The isolated wing method presented in NACA TN 1350 predicts the twist distribution and camber shape necessary to obtain an almost uniform spanwise loading over most of the blade span when tested at a cascade configuration of inlet-air angle of 60° and solidity 1.0.

2. A linear twist distribution is sufficient to maintain an almost uniform loading over at least the center 50 percent of the blade semispan for inlet-air angles ranging from 0° to 60° at a solidity of 1.0 and from solidities of 1.0 to 1.5 at an inlet-air angle of 45°, over the angle-of-attack ranges tested.

3. The twist distribution necessary to obtain a constant effective angle of attack and spanwise loading is practically independent of the variations in blade loading and blade-loading distribution investigated herein.

4. For the region in which uniform spanwise loading was achieved, the swept blades in cascade have streamwise blade surface pressure coefficients which, when converted to normal section pressure distributions,

are similar to those that would be obtained if the normal configuration of blade section, inlet angle, and solidity were tested as a cascade of unswept blades.

5. Pressure coefficients in the region where pressure distributions were measured (the center 50 percent of the semispan of blade 2A and the center 50 percent of the span of blade 2B) decrease proceeding downstream along lines of constant chordwise position.

6. In the region in which the agreement found between the low-speed swept normal and unswept estimated pressure distributions remains valid at high Mach numbers, the Mach number limit for efficient operation of the swept blade would be approximately that of the normal section, at the normal inlet angle and solidity, divided by the cosine of the sweep angle.

7. The angle-of-attack operating range of a uniformly loaded 45° sweptback blade in cascade compared favorably with that of unswept blades.

8. The half-arrow-shaped swept-blade tests indicated that pressure distributions similar in shape to those of the arrow-shaped swept blade tests occurred at approximately 3° higher angles of attack and that at these higher angles of attack lower convex surface pressure coefficients were obtained.

Langley Aeronautical Laboratory,
National Advisory Committee for Aeronautics,
Langley Field, Va., November 23, 1953.

APPENDIX A

DERIVATION OF THE RELATIONSHIPS BETWEEN THE NORMAL AND THE STREAMWISE CASCADE PARAMETERS

A plan and two elevation views of a cascade of untwisted swept blades is shown in figure 25. When the following derived expressions are applied to the cascade of this investigation, it is necessary to assume that the effect of blade twist on the parameters is negligible. This assumption is substantiated by the excellent shape agreement of the pressure distributions taken in the center 50 percent of the semispan.

From figure 25, the following relations may be seen:

$$g_n' = g' \cos \Lambda \tag{A1}$$

$$c_n = c \cos \Lambda \tag{A2}$$

$$m_n = m \cos \Lambda \tag{A3}$$

$$g' = g \sin(\beta_1 - \alpha) \tag{A4}$$

$$h = g \cos(\beta_1 - \alpha) \tag{A5}$$

$$\tan \alpha = \frac{k}{g'} \tag{A6}$$

$$\tan(\beta_1 - \alpha) = \frac{g'}{h} \tag{A7}$$

$$\tan(\beta_1 - \alpha - \beta_2) = \frac{r}{m} \tag{A8}$$

$$g_n = \sqrt{h^2 + (g_n')^2} \tag{A9}$$

Solidity.- The ratio of

$$\frac{\sigma_n}{\sigma} = \frac{c_n}{c}\frac{g}{g_n} \tag{A10}$$

Combining relations (A1), (A2), (A4), (A5), (A9), and (A10) results in

$$\sigma_n = \frac{\sigma}{\sqrt{\frac{\cos^2(\beta_1 - \alpha)}{\cos^2\Lambda} + \sin^2(\beta_1 - \alpha)}} \tag{A11}$$

Angle of attack.- From figure 25(c),

$$\alpha_n = \tan^{-1}\frac{k}{g_n'} \tag{A12}$$

Substituting expressions (A1) and (A6) into equation (A12) results in

$$\alpha_n = \tan^{-1}\frac{\tan\alpha}{\cos\Lambda} \tag{A13}$$

Inlet air angle.- From figure 25(c),

$$\beta_{1,n} - \alpha_n = \tan^{-1}\frac{g_n'}{h} \tag{A14}$$

Substituting equations (A1) and (A7) into equation (A14) results in

$$\beta_{1,n} = \tan^{-1}\left[\tan(\beta_1 - \alpha)\cos\Lambda\right] + \alpha_n \tag{A15}$$

Turning angle.- From figure 25(c),

$$\beta_{1,n} - \alpha_n - \beta_{2,n} = \tan^{-1} \frac{r}{m_n} \tag{A16}$$

Substituting equations (A3) and (A8) into equation (A16) results in

$$\beta_{1,n} - \alpha_n - \beta_{2,n} = \tan^{-1} \frac{\tan(\beta_1 - \alpha - \beta_2)}{\cos \Lambda} \tag{A17}$$

and since $(\beta_{1,n} - \beta_{2,n}) = \theta_n$ and $(\beta_1 - \beta_2) = \theta$,

$$\theta_n = \tan^{-1} \frac{\tan(\theta - \alpha)}{\cos \Lambda} + \alpha_n \tag{A18}$$

Blade section camber and thickness.- Inasmuch as blade section camber and thickness are affected only by the decrease in chord from streamwise to normal, the following relations apply:

$$\left(c_{l,o}\right)_n = \frac{c_{l,o}}{\cos \Lambda} \tag{A19}$$

and

$$\left(\frac{t}{c}\right)_n = \frac{t/c}{\cos \Lambda} \tag{A20}$$

APPENDIX B

CONVERSION OF STREAMWISE PRESSURE COEFFICIENT TO PRESSURE COEFFICIENT BASED ON CONDITIONS NORMAL TO BLADE LEADING EDGE

For incompressible flow,

$$S = \frac{P - p_l}{P - p_1} = \frac{q_l}{q_1} \tag{B1}$$

and

$$S_n = \frac{P_n - p_l}{P_n - p_1} = \frac{q_{l_n}}{q_{1_n}} \tag{B2}$$

Therefore,

$$\frac{q_{l_n}}{q_{1_n}} = \frac{q_{l_n} - q_{1_n}}{q_{1_n}} + 1$$

$$= \frac{q_l - q_1}{q_{1_n}} + 1$$

$$= \frac{\frac{q_l}{q_1} - 1}{\cos^2\Lambda} + 1$$

$$= \frac{q_l}{q_1}\left(1 + \tan^2\Lambda\right) - \tan^2\Lambda$$

Hence,

$$S_n = S\left(1 + \tan^2\Lambda\right) - \tan^2\Lambda \tag{B3}$$

REFERENCES

1. Savage, Melvyn, Erwin, John R., and Whitley, Robert P.: Investigation of an Axial-Flow Compressor Rotor Having NACA High-Speed Blade Sections (A_2I_{8b} Series) at Mean Radius Relative Inlet Mach Numbers up to 1.13. NACA RM L53G02, 1953.

2. Lieblein, Seymour, Lewis, George W., Jr., and Sandercock, Donald M.: Experimental Investigation of an Axial-Flow Compressor Inlet Stage Operating at Transonic Relative Inlet Mach Numbers. I - Over-All Performance of Stage With Transonic Rotor and Subsonic Stators Up to Rotor Relative Inlet Mach Numbers of 1.1. NACA RM E52A24, 1952.

3. Jones, Robert T.: Estimated Lift-Drag Ratios at Supersonic Speed. NACA TN 1350, 1947.

4. Erwin, John R., and Yacobi, Laura A.: Method of Estimating the Incompressible-Flow Pressure Distribution of Compressor Blade Sections at Design Angle of Attack. NACA RM L53F17, 1953.

5. Erwin, John R., and Emery, James C.: Effect of Tunnel Configuration and Testing Technique on Cascade Performance. NACA Rep. 1016, 1951. (Supersedes NACA TN 2028.)

6. Herrig, L. Joseph, Emery, James C., and Erwin, John R.: Systematic Two-Dimensional Cascade Tests of NACA 65-Series Compressor Blades at Low Speeds. NACA RM L51G31, 1951.

7. Erwin, John R., Savage, Melvyn, and Emery, James C.: Two-Dimensional Low-Speed Cascade Investigation of NACA Compressor Blade Sections Having a Systematic Variation in Mean-Line Loading. NACA RM L53I30b, 1953.

8. Gothert, B.: High-Speed Measurements on a Swept-Back Wing (Sweepback Angle $\varphi = 35^{\circ}$). NACA TM 1102, 1947.

TABLE 1.- STREAMWISE BLADE COORDINATES

[Stations and ordinates are in percent chord]

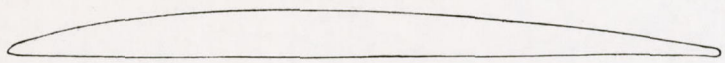

Streamwise section - Blade 1

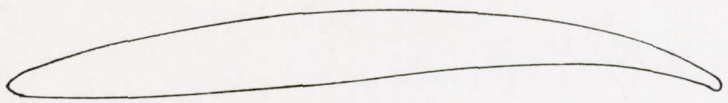

Streamwise section - Blades 2A and 2B

Blade 1			Blades 2A and 2B		
Station	Upper	Lower	Station	Upper	Lower
0	0	0	0	0	0
.5	.72	-.41	.5	.97	-.62
.75	.87	-.47	.75	1.16	-.73
1.25	1.15	-.53	1.25	1.46	-.90
2.5	1.69	-.66	2.5	2.10	-1.18
5	2.50	-.65	5	3.03	-1.40
7.5	3.16	-.65	7.5	3.81	-1.52
10	3.72	-.65	10	4.55	-1.59
15	4.55	-.66	15	5.87	-1.58
20	5.14	-.68	20	7.00	-1.35
25	5.61	-.71	25	7.98	-1.08
30	5.94	-.76	30	8.79	-.77
35	6.13	-.82	35	9.47	-.39
40	6.24	-.83	40	10.08	.03
45	6.24	-.83	45	10.57	.50
50	6.12	-.74	50	10.79	.97
55	5.90	-.69	55	10.84	1.50
60	5.51	-.56	60	10.72	2.03
65	5.10	-.42	65	10.38	2.53
70	4.64	-.29	70	9.88	2.90
75	4.12	-.16	75	9.20	3.04
80	3.61	-.10	80	8.36	3.04
85	3.07	-.04	85	7.20	2.76
90	2.40	-.10	90	5.70	2.06
95	1.67	-.24	95	3.83	1.01
100	0	0	100	0	0
L.E. radius slope = 0.254; L.E. radius = 0.639 T.E. radius slope = 0.221; T.E. radius = 1.000			L.E. radius slope = 0.159; L.E. radius = 0.639 T.E. radius slope = 0.640; T.E. radius = 1.000		

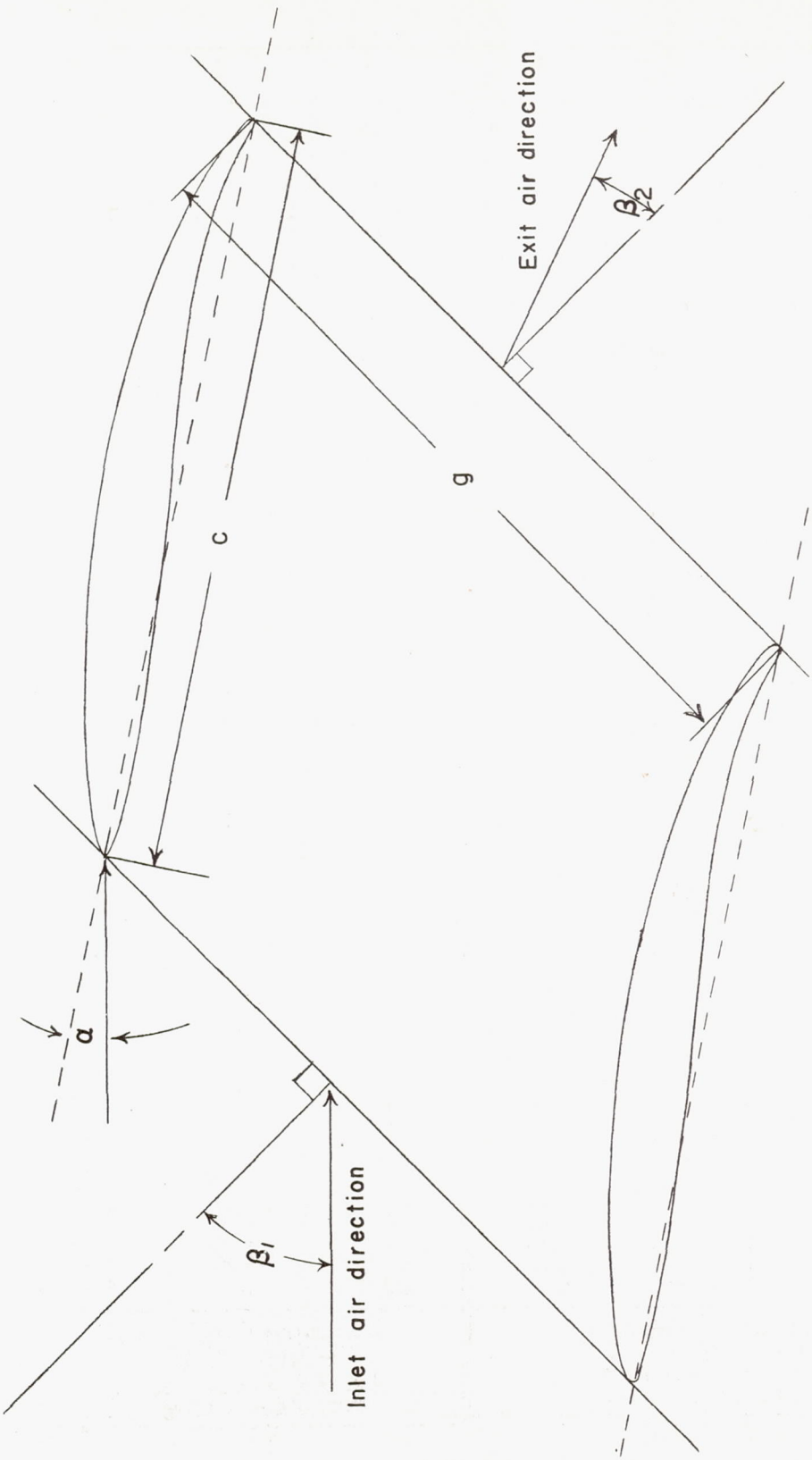

Figure 1.- Cascade notation.

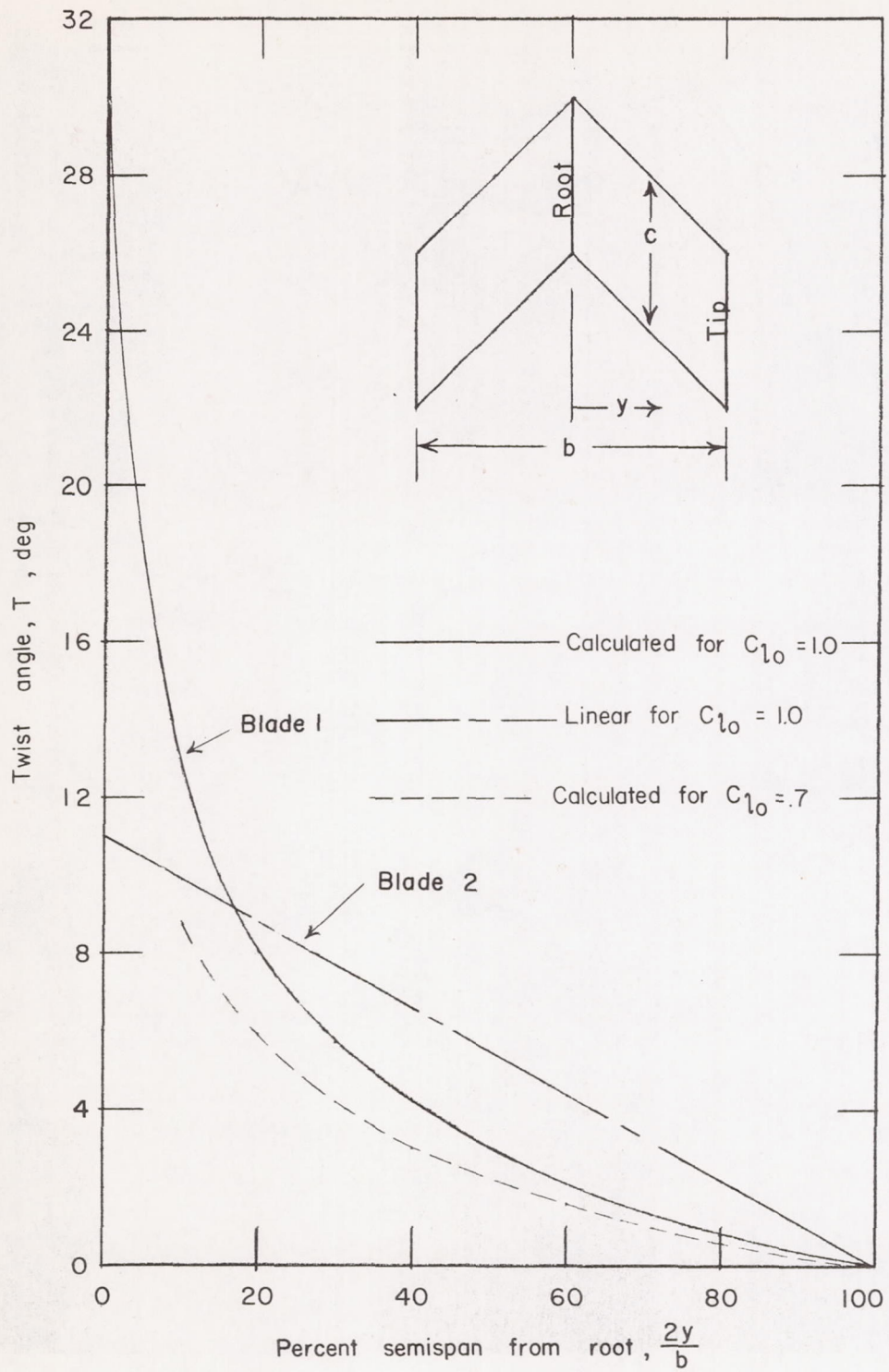

Figure 2.- Twist distributions calculated by the method of reference 3 for lift coefficients of 1.0 and 0.7 and a linear twist distribution chosen to conform closely to the twist calculated for C_{l_o} = 1.0.

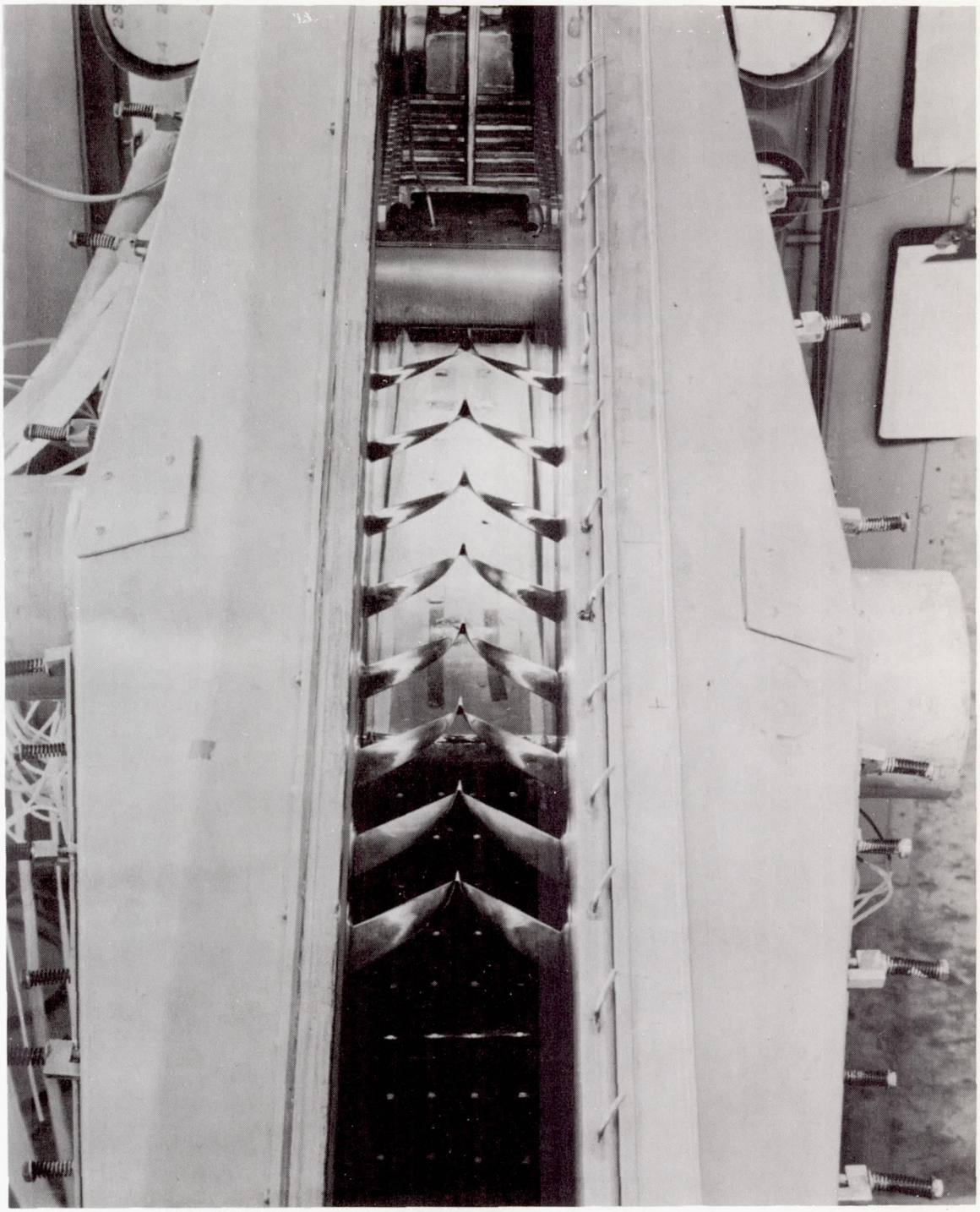

L-67556

Figure 3.- Swept blade 1 mounted in the 5-inch cascade tunnel.

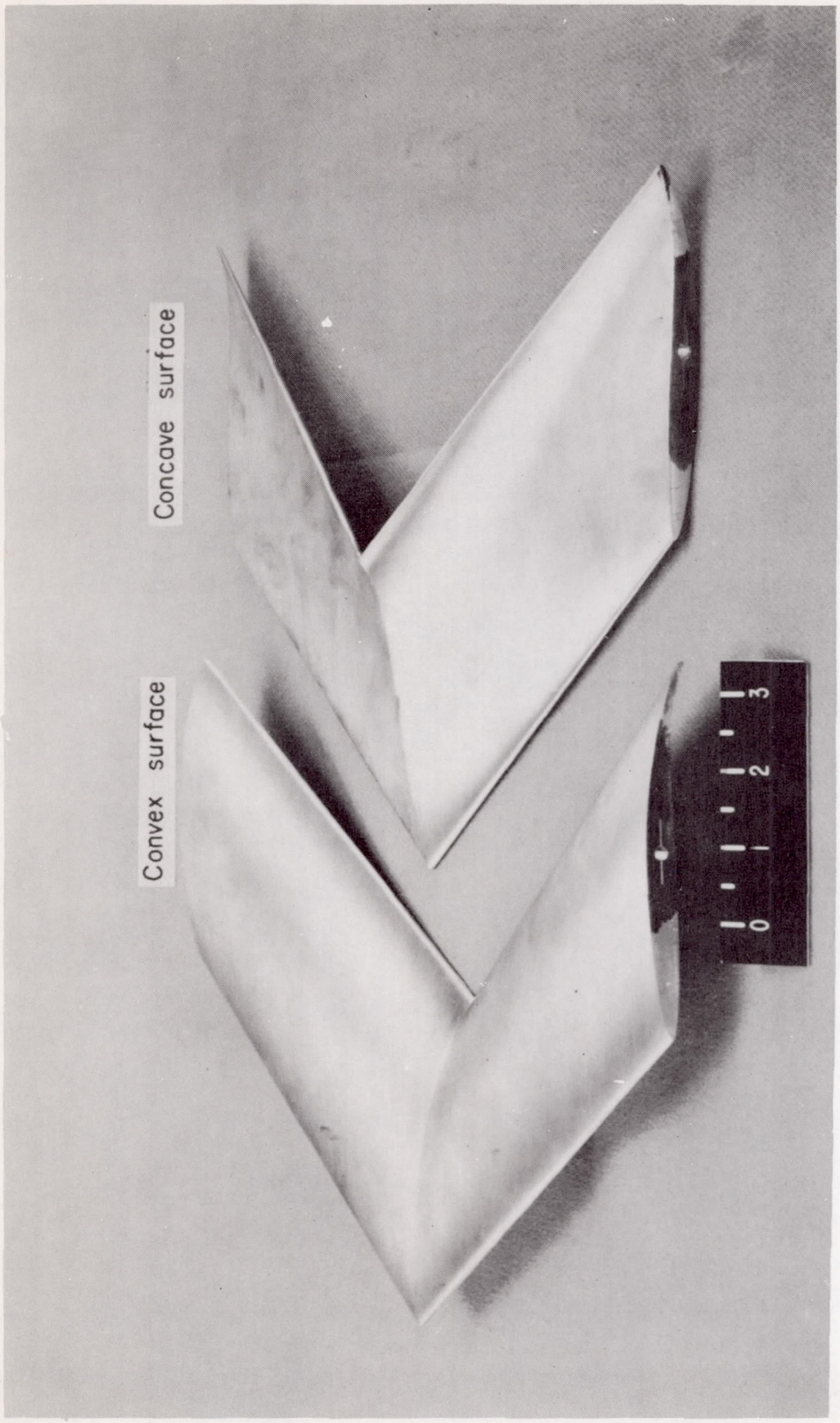

L-70126.1

Figure 4.- Swept blade 2A.

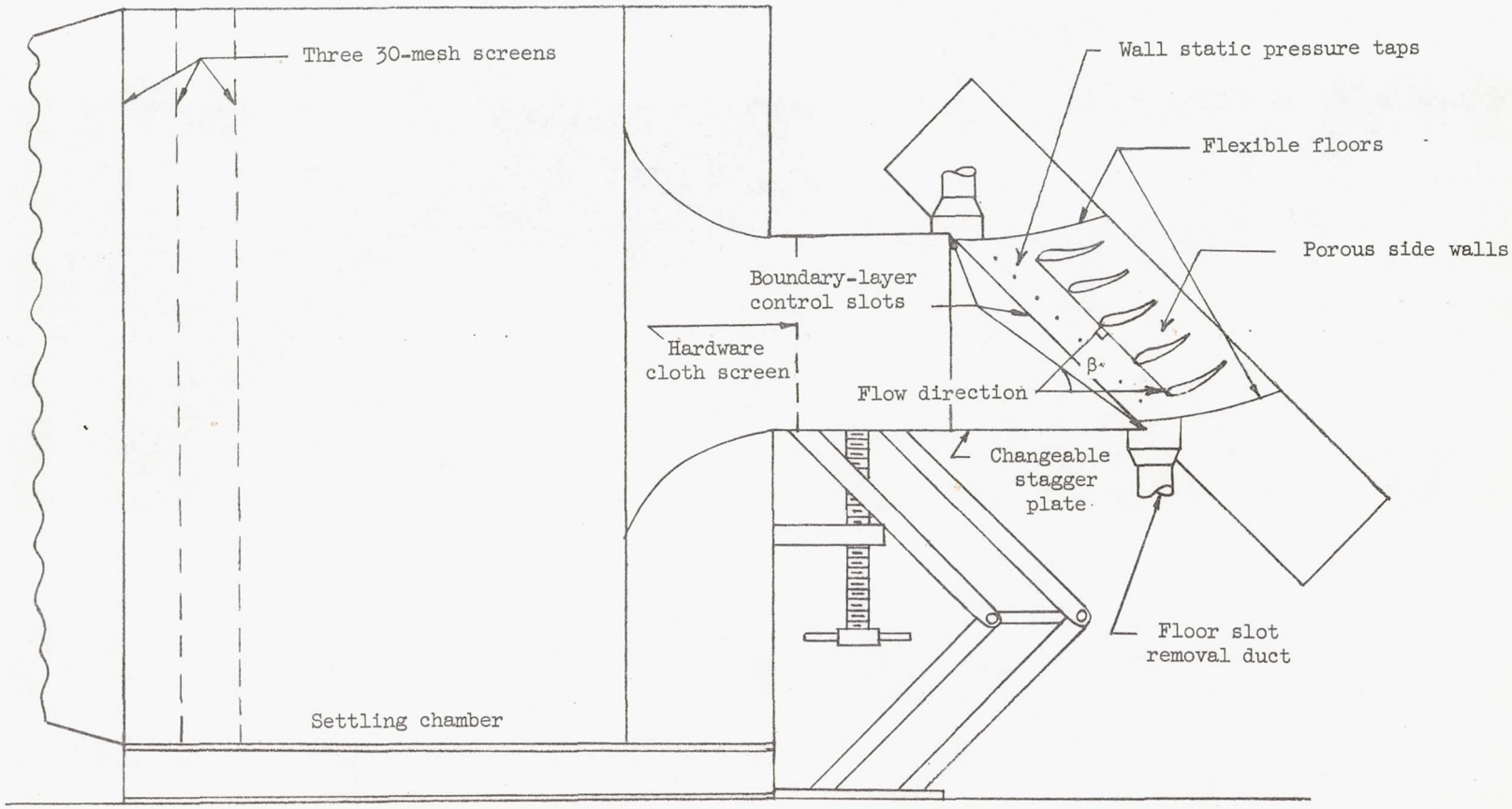

Figure 5.- Vertical cross section of two-dimensional low-speed cascade tunnel.

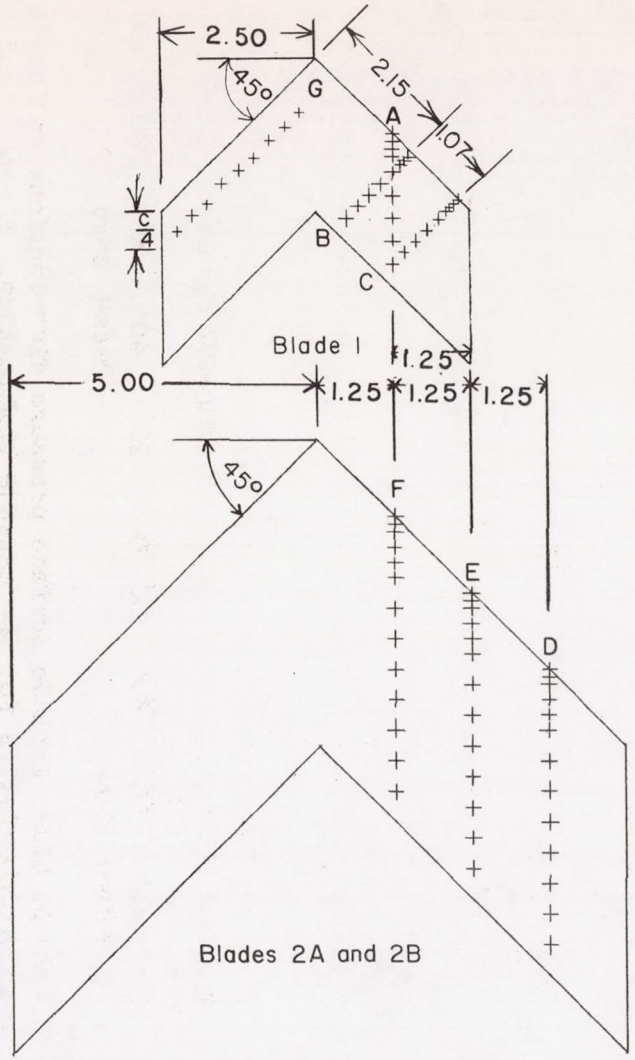

Orifice Locations		
Blade 1		Blades 2A and 2B
A, B, C, Percent chord	G, Percent semispan	D, E, F, Percent chord
0	10.4	0
5	20.3	2 1/2
10	30.2	5
15	40.1	10
25	50.0	15
40	59.9	20
55	69.8	30
70	79.7	40
85	89.6	50
		60
		70
		80
		90

Figure 6.- Blade surface static pressure tap locations on upper and lower surfaces of blades 1 and 2. All dimensions are in inches.

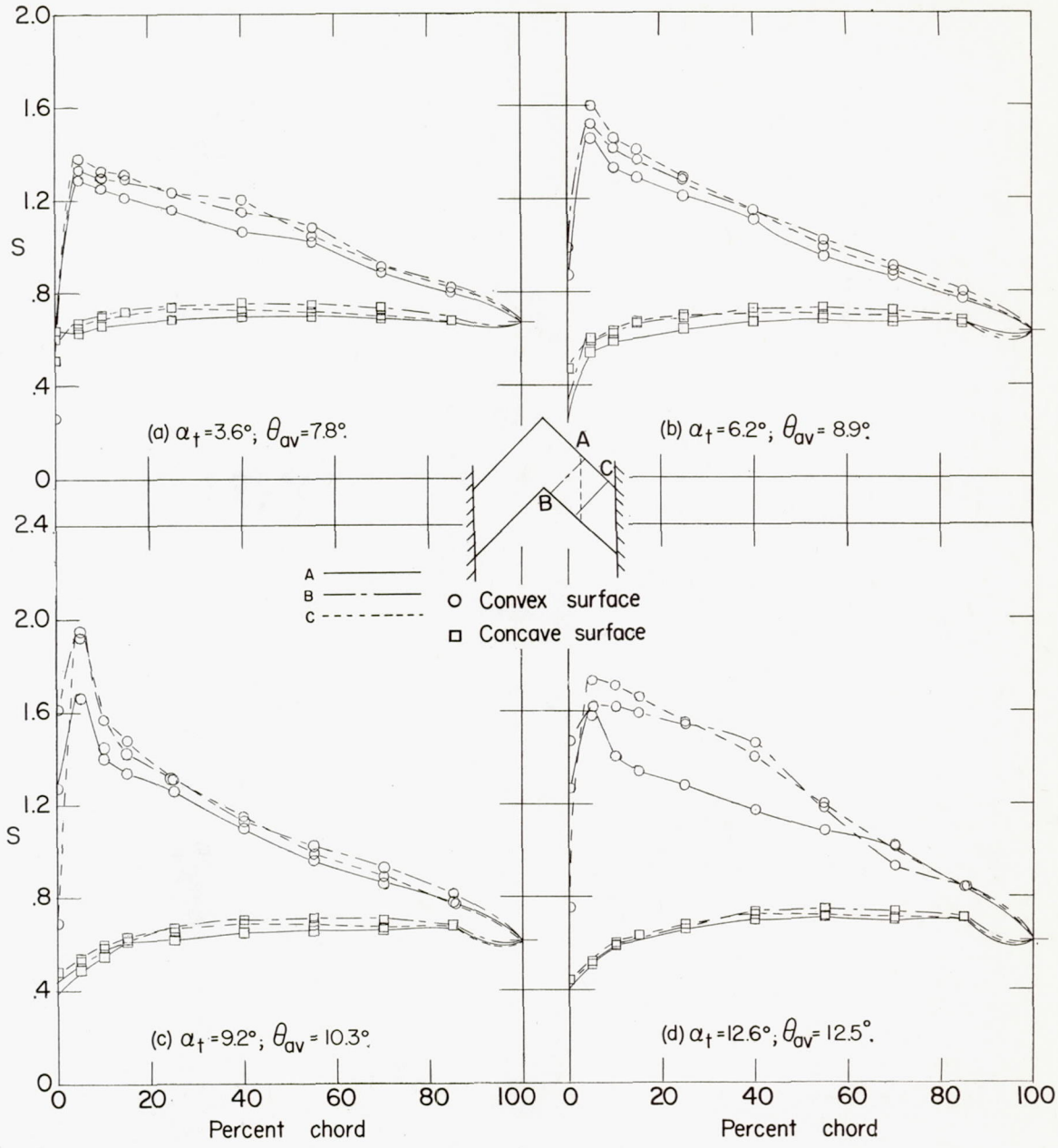

Figure 7.- Swept blade 1 blade surface pressure distributions and blade section characteristics for the cascade combination, $\beta = 60^{\circ}$ and $\sigma = 1.0$.

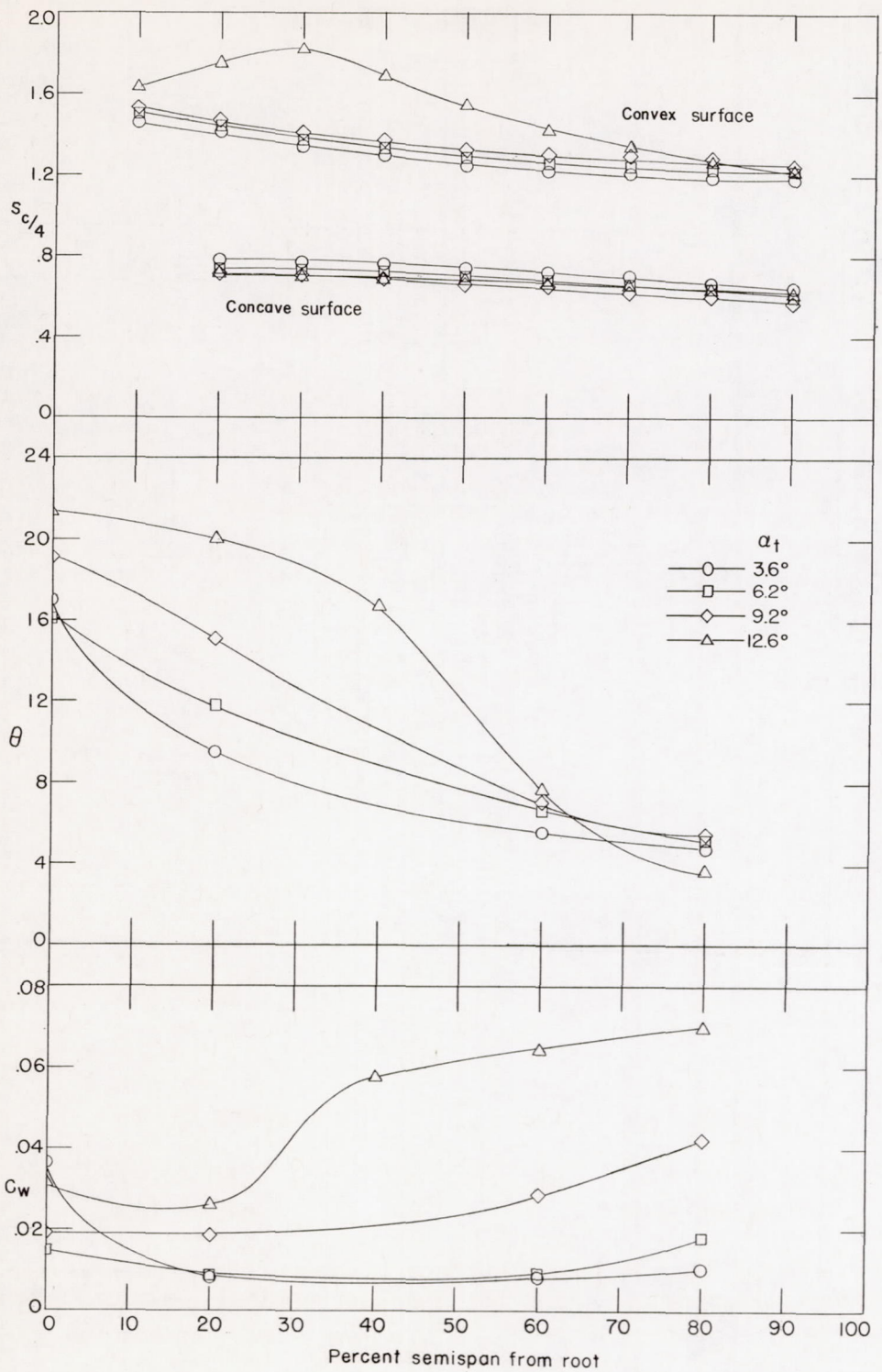

(e) Section characteristics.

Figure 7.- Continued.

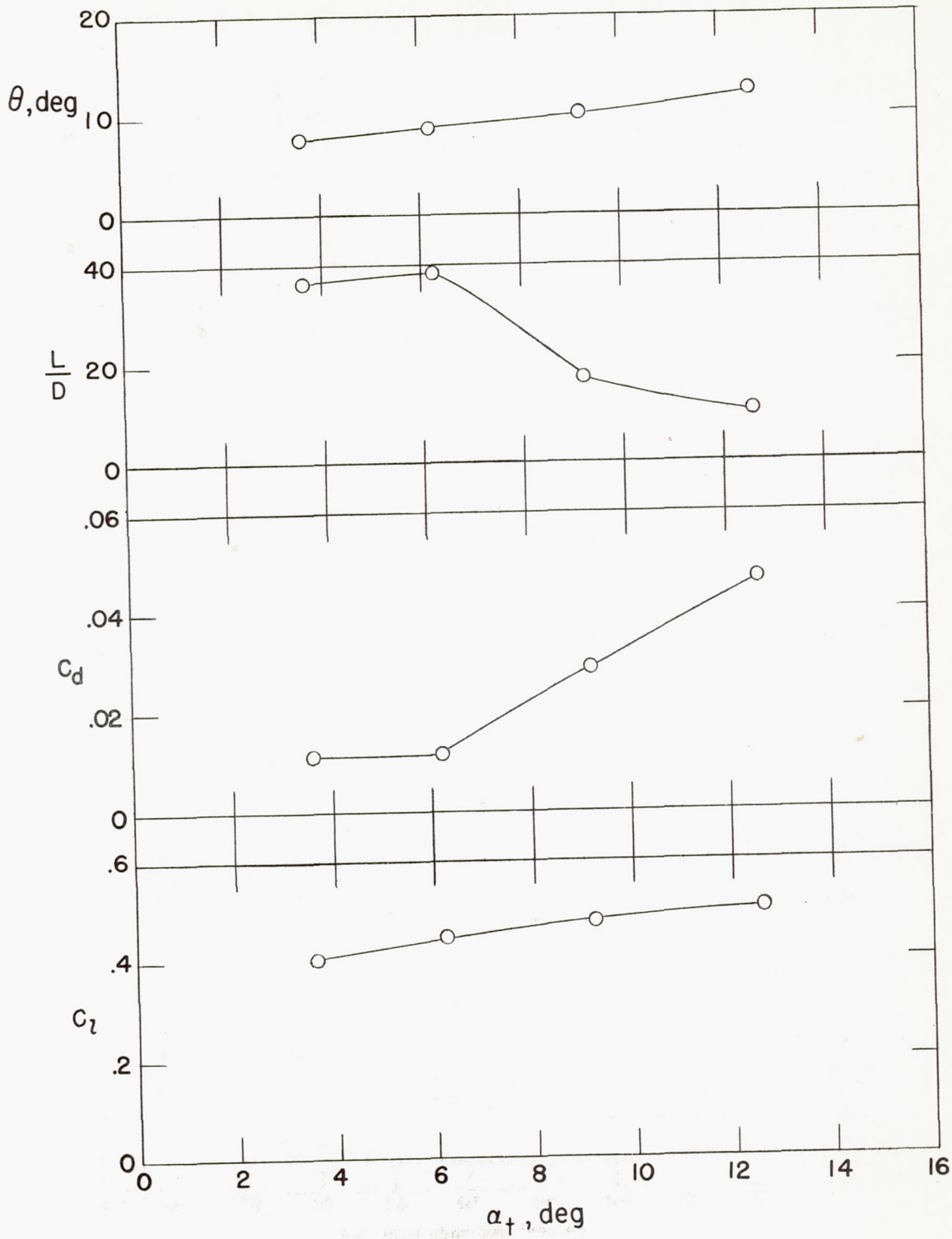

(f) Average blade characteristics.

Figure 7.- Concluded.

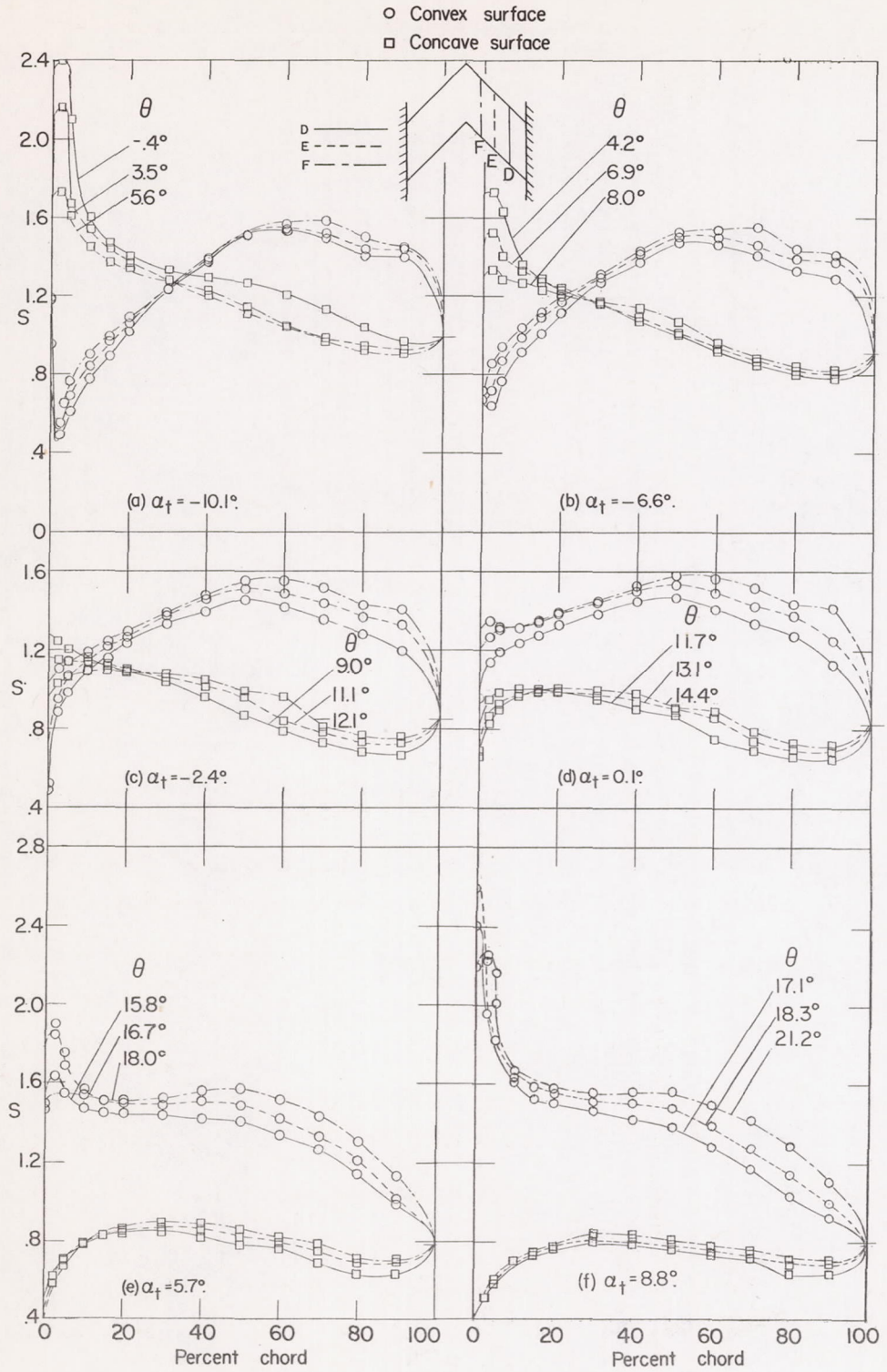

Figure 8.- Swept blade 2A blade surface pressure distributions and blade section characteristics for the cascade combination, $\beta = 30^{\circ}$ and $\sigma = 1.0$.

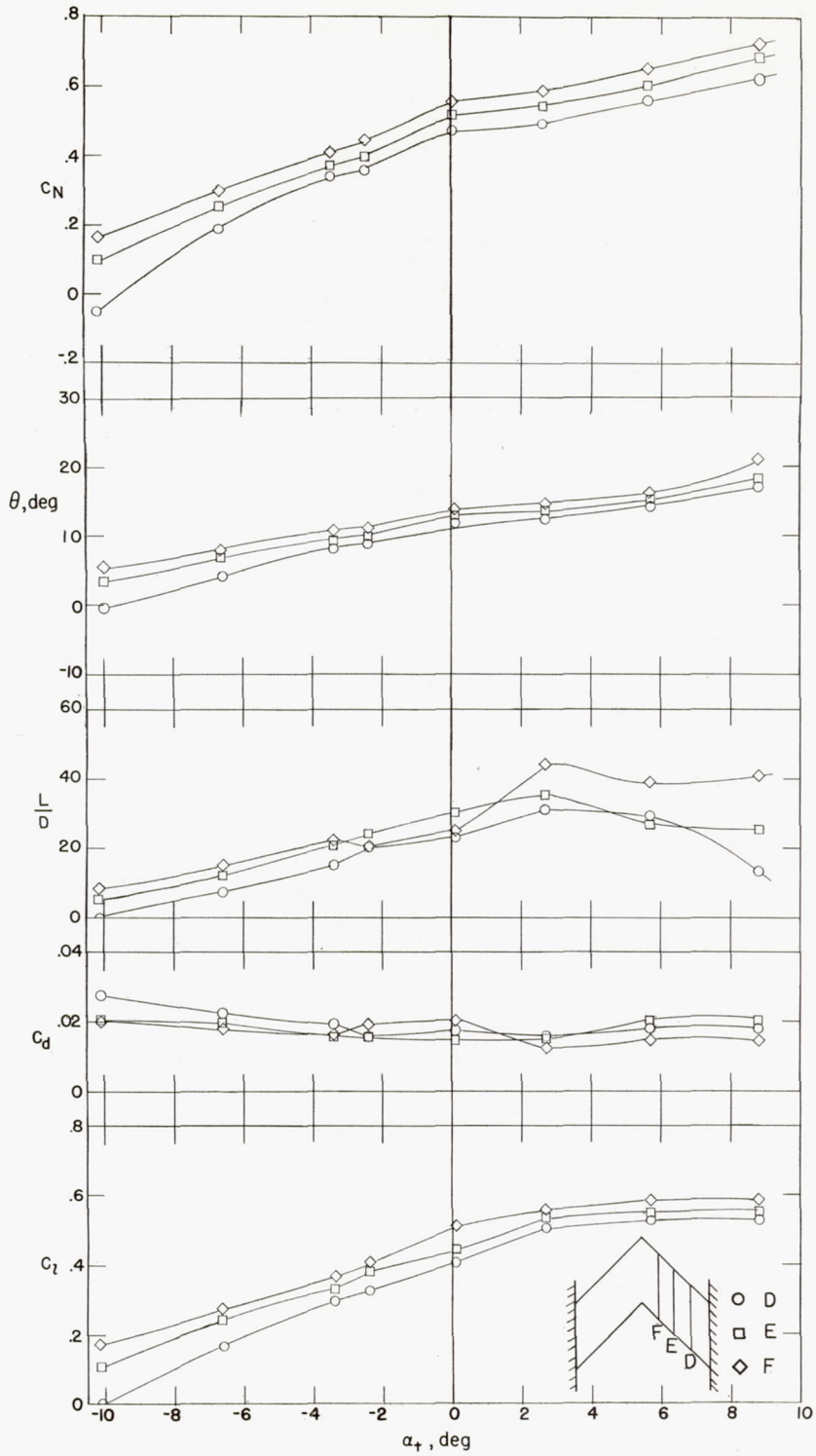

(g) Section characteristics.

Figure 8.- Concluded.

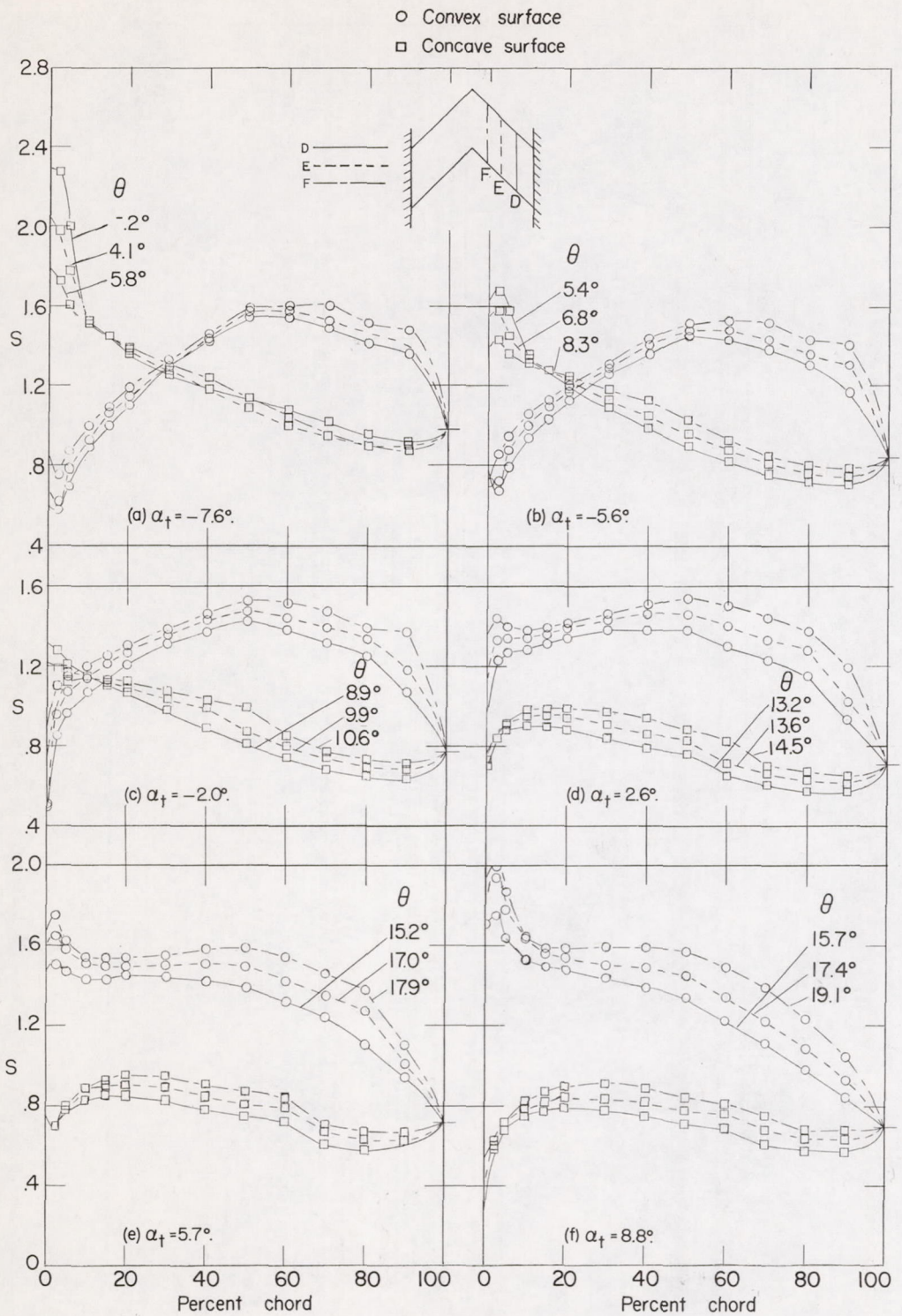

Figure 9.- Swept blade 2A blade surface pressure distributions and blade section characteristics for the cascade combination, $\beta = 45^{\circ}$ and $\sigma = 1.0$.

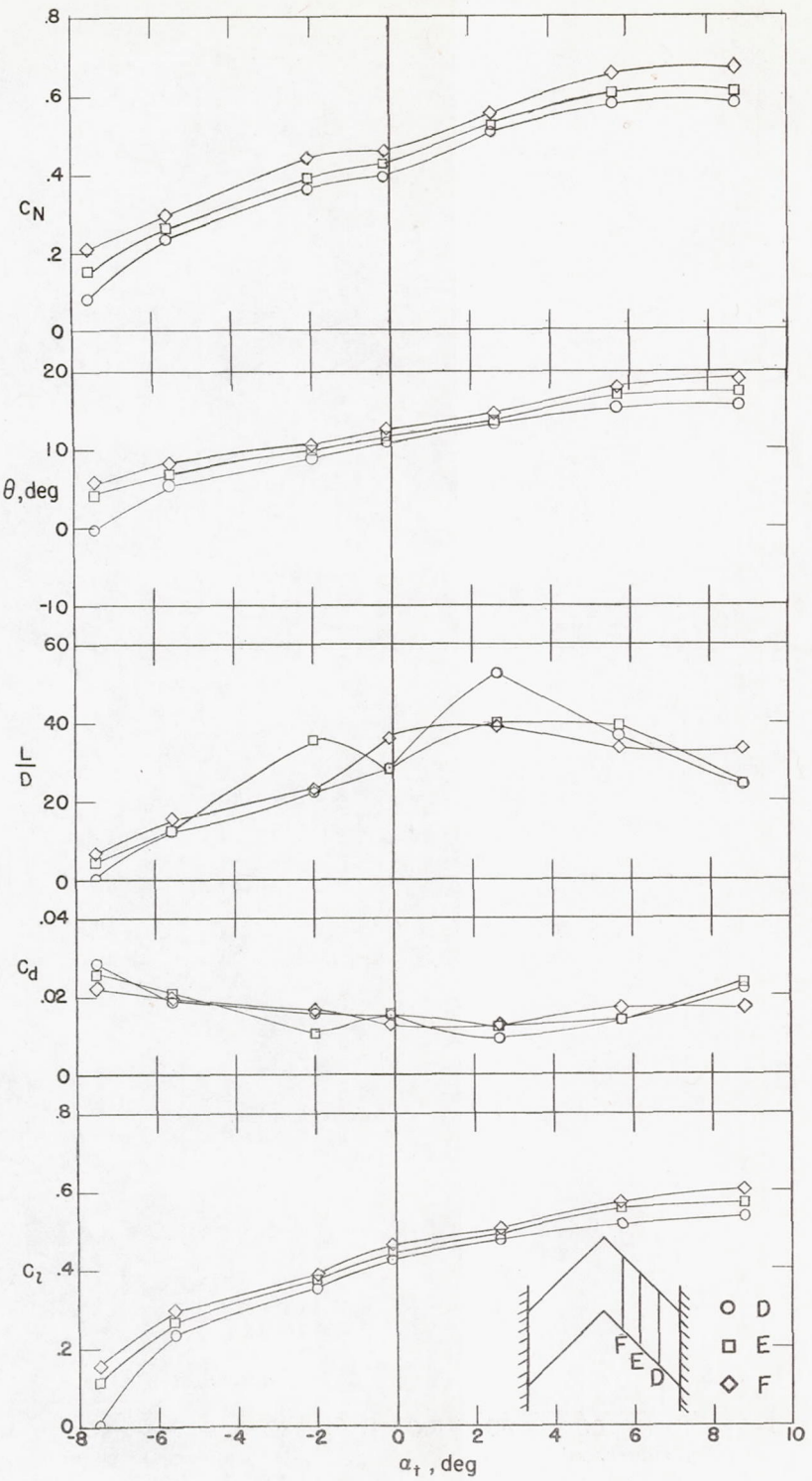

(g) Section characteristics.

Figure 9.- Concluded.

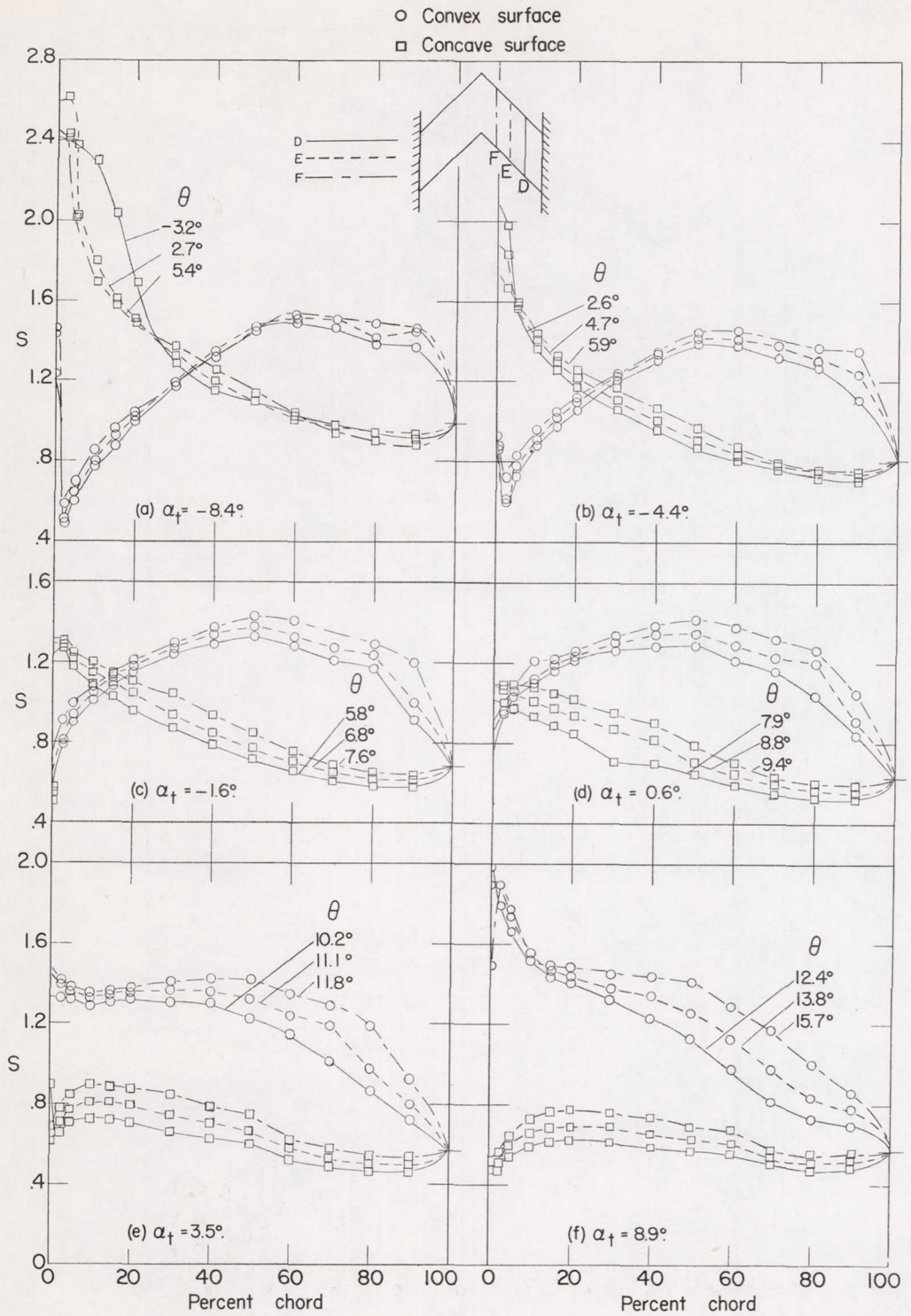

Figure 10.- Swept blade 2A blade surface pressure distributions and blade section characteristics for the cascade combination, $\beta = 60^\circ$ and $\sigma = 1.0$.

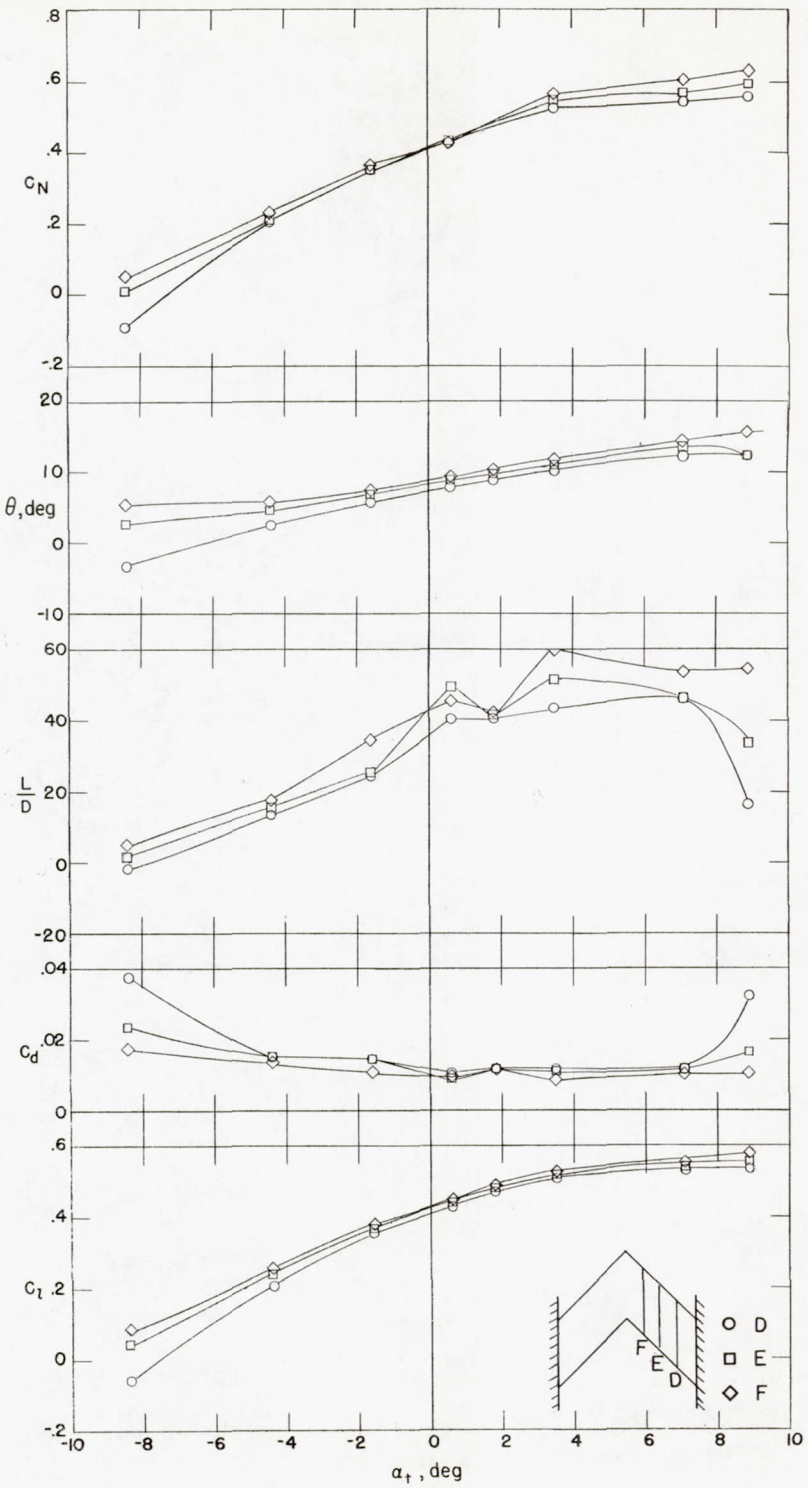

(g) Section characteristics.

Figure 10.- Concluded.

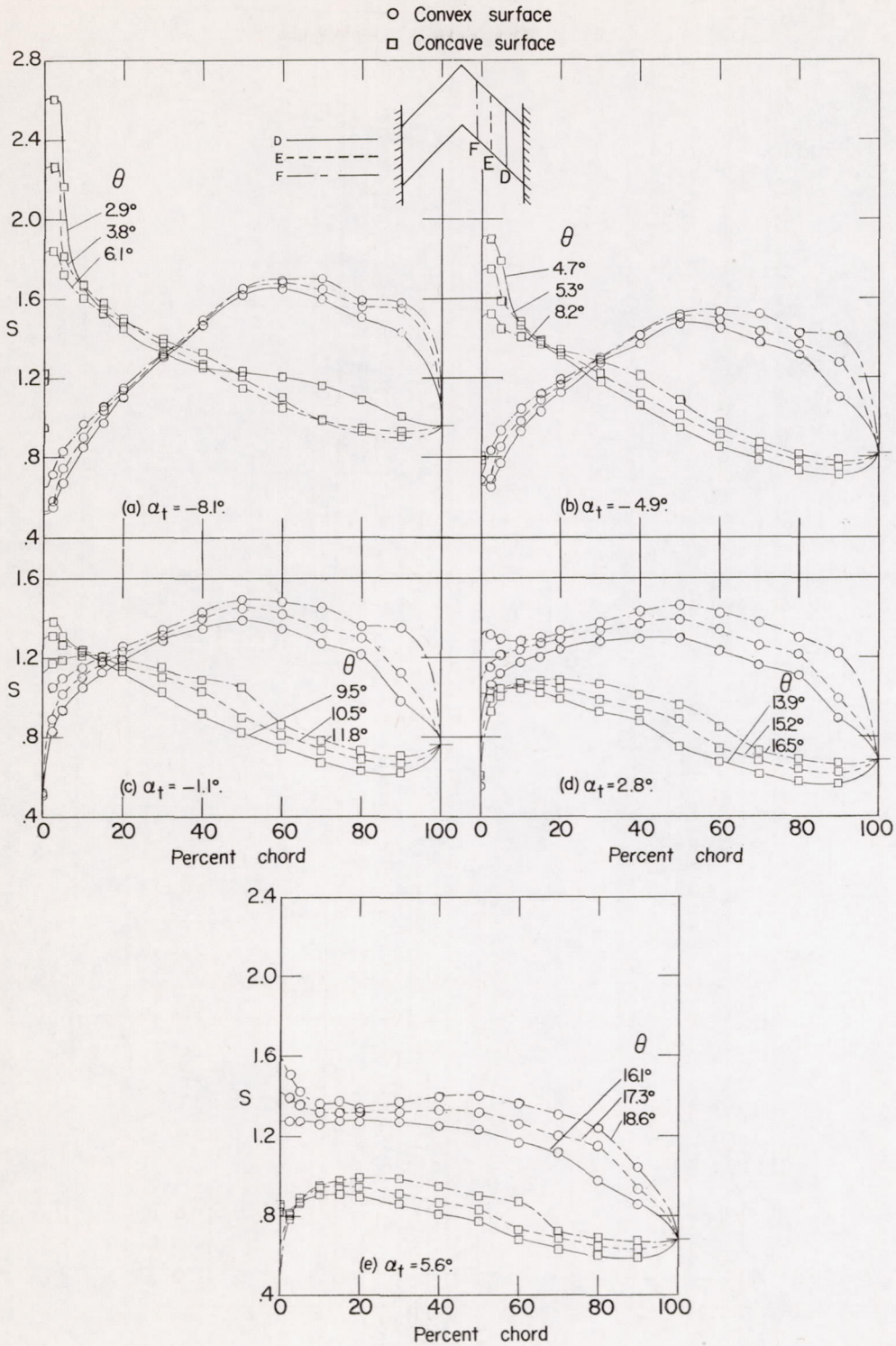

Figure 11.- Swept blade 2A blade surface pressure distributions and blade section characteristics for the cascade combination, $\beta = 45^0$ and $\sigma = 1.25$.

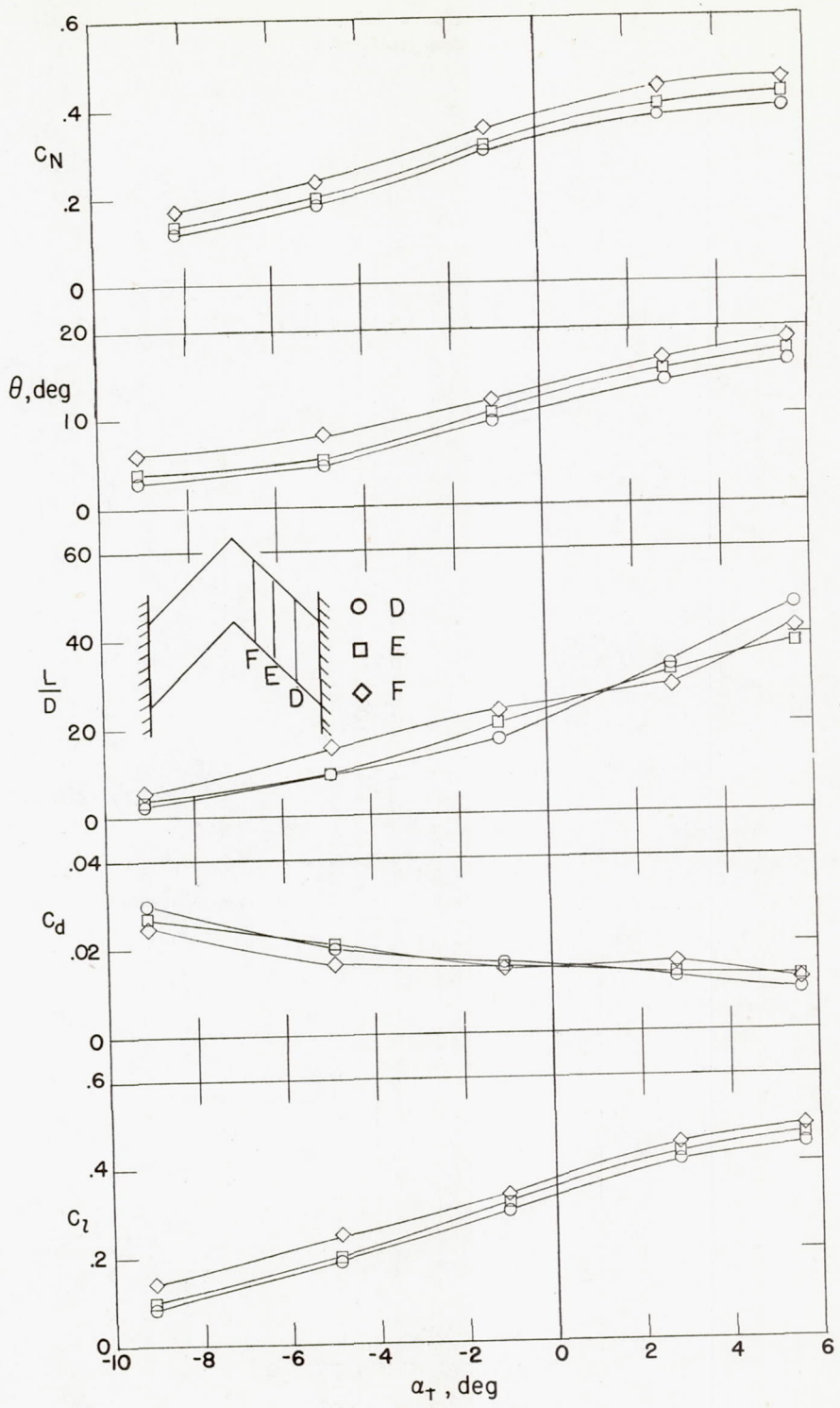

(f) Section characteristics.

Figure 11.- Concluded.

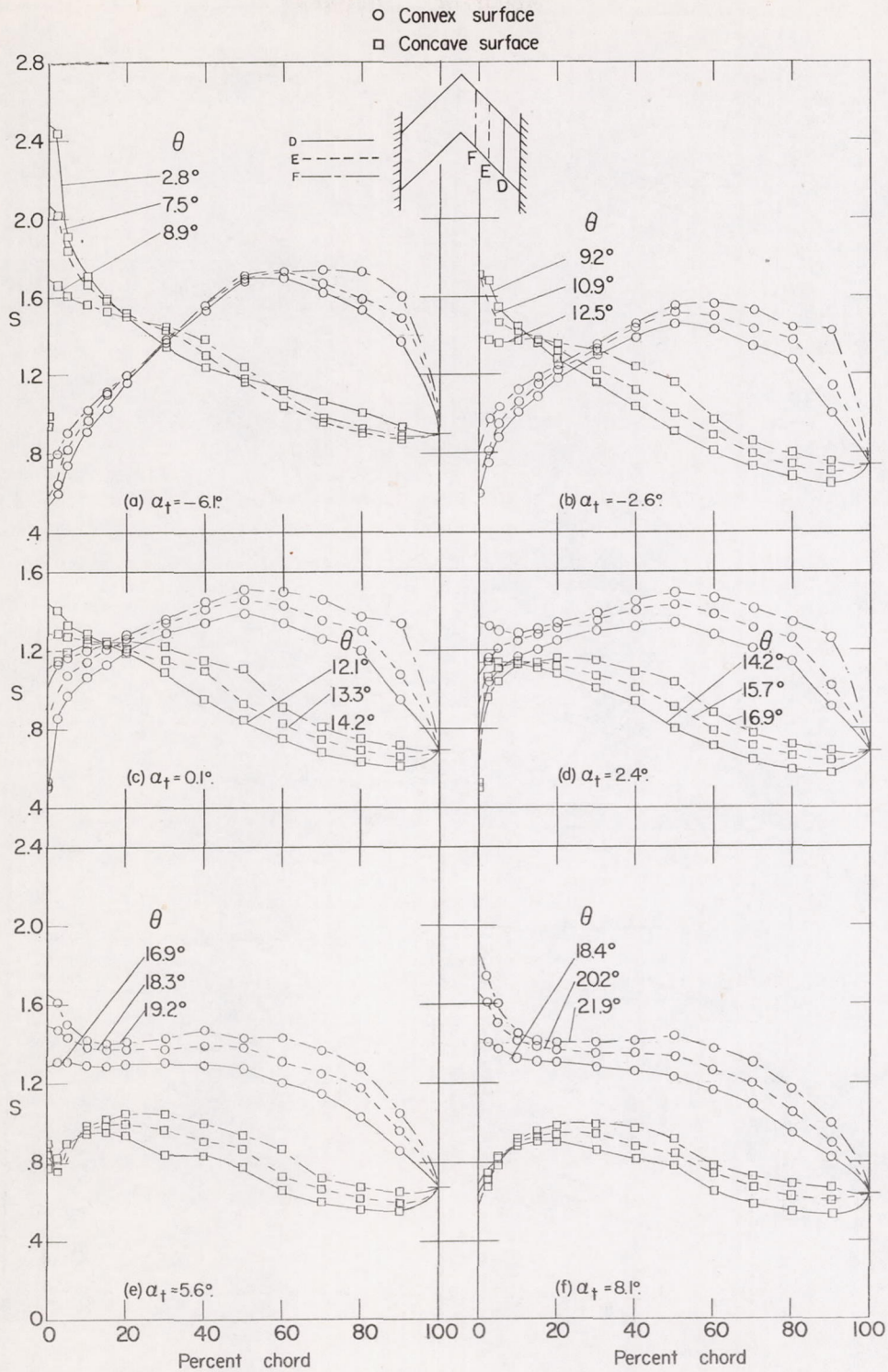

Figure 12.- Swept blade 2A blade surface pressure distributions and blade section characteristics for the cascade combination, $\beta = 45^\circ$ and $\sigma = 1.5$.

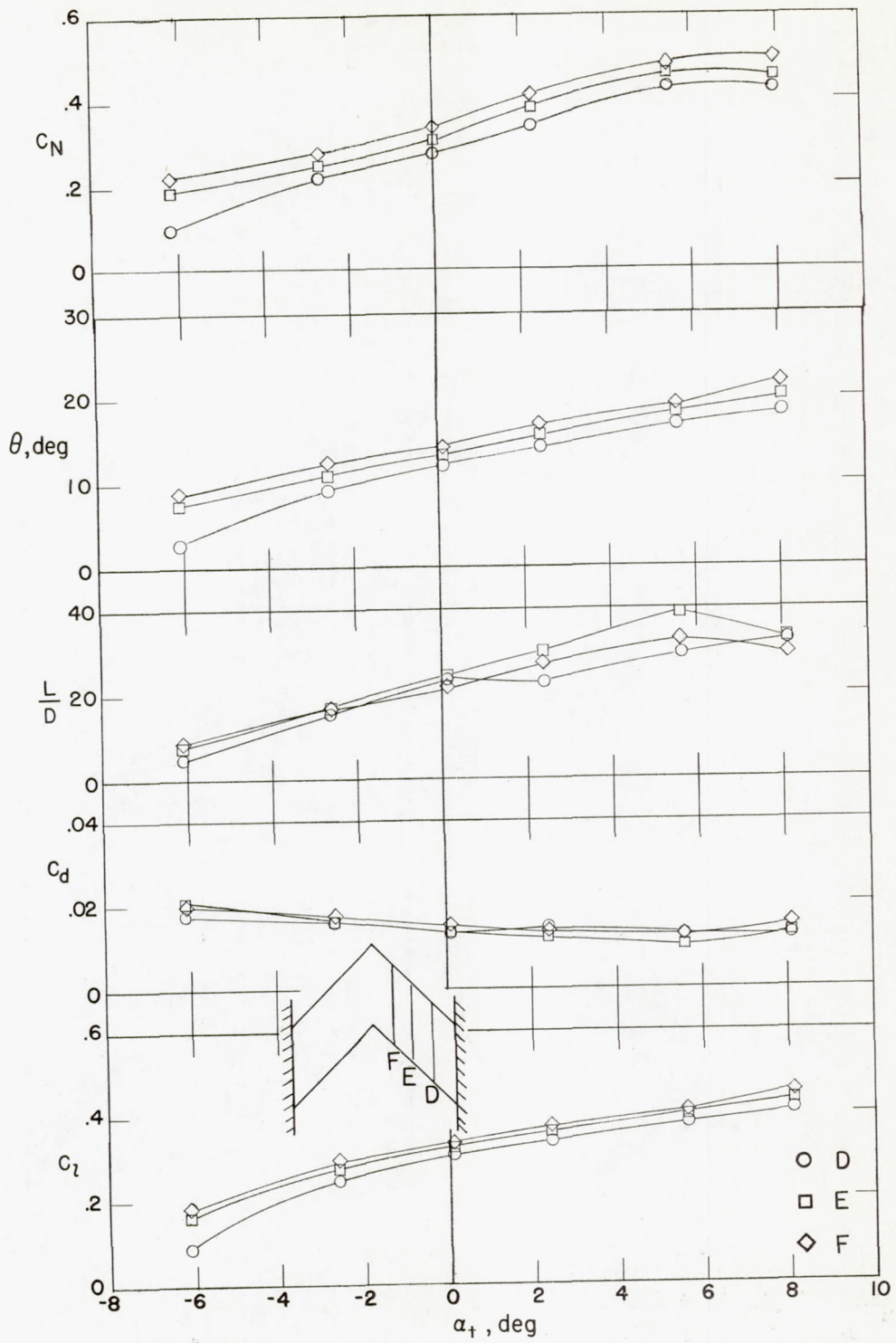

(g) Section characteristics.

Figure 12.- Concluded.

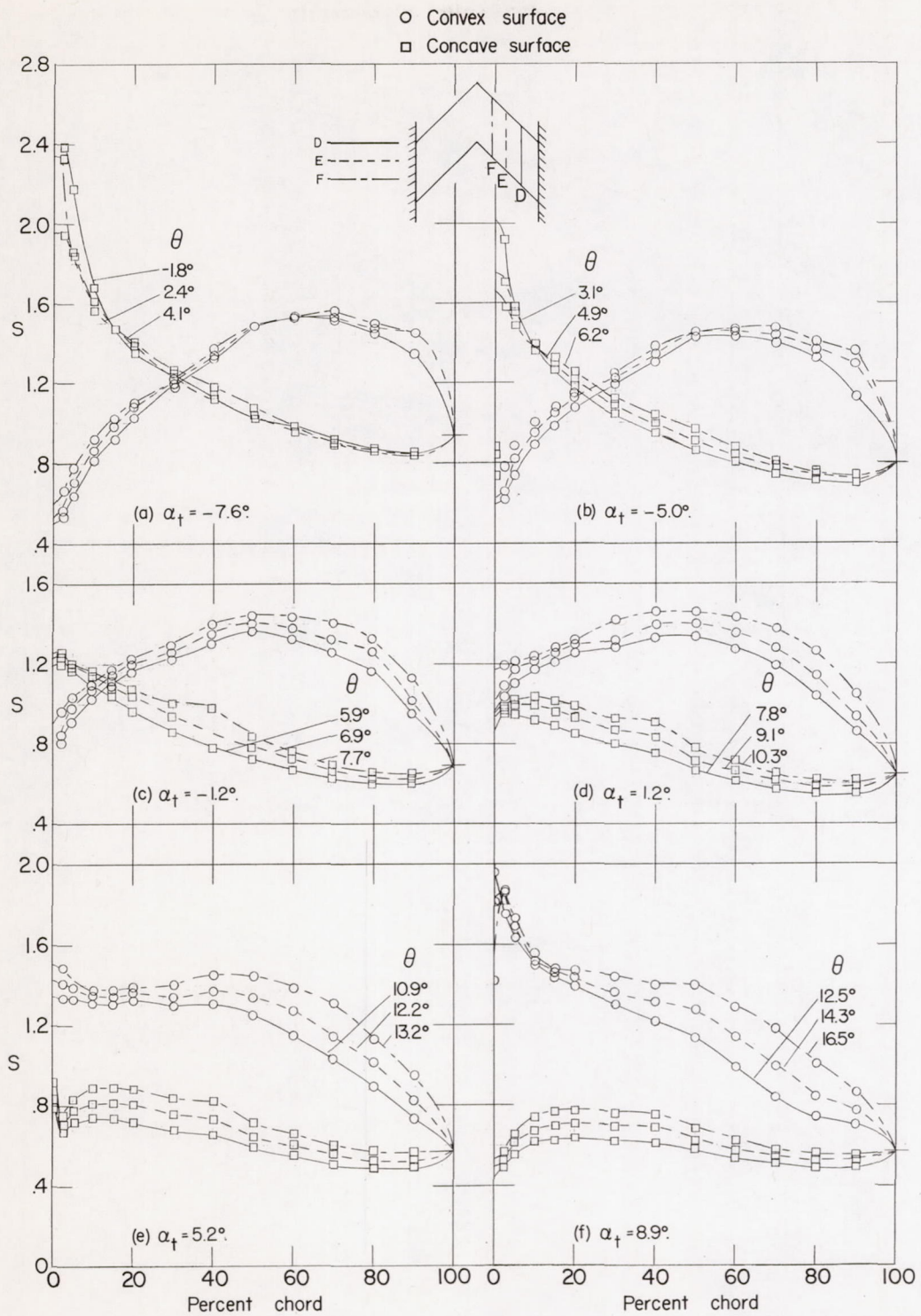

Figure 13.- Swept blade 2A blade surface pressure distributions and blade section characteristics for the cascade combination, $\beta = 60^\circ$ and $\sigma = 1.0$ with roughness added.

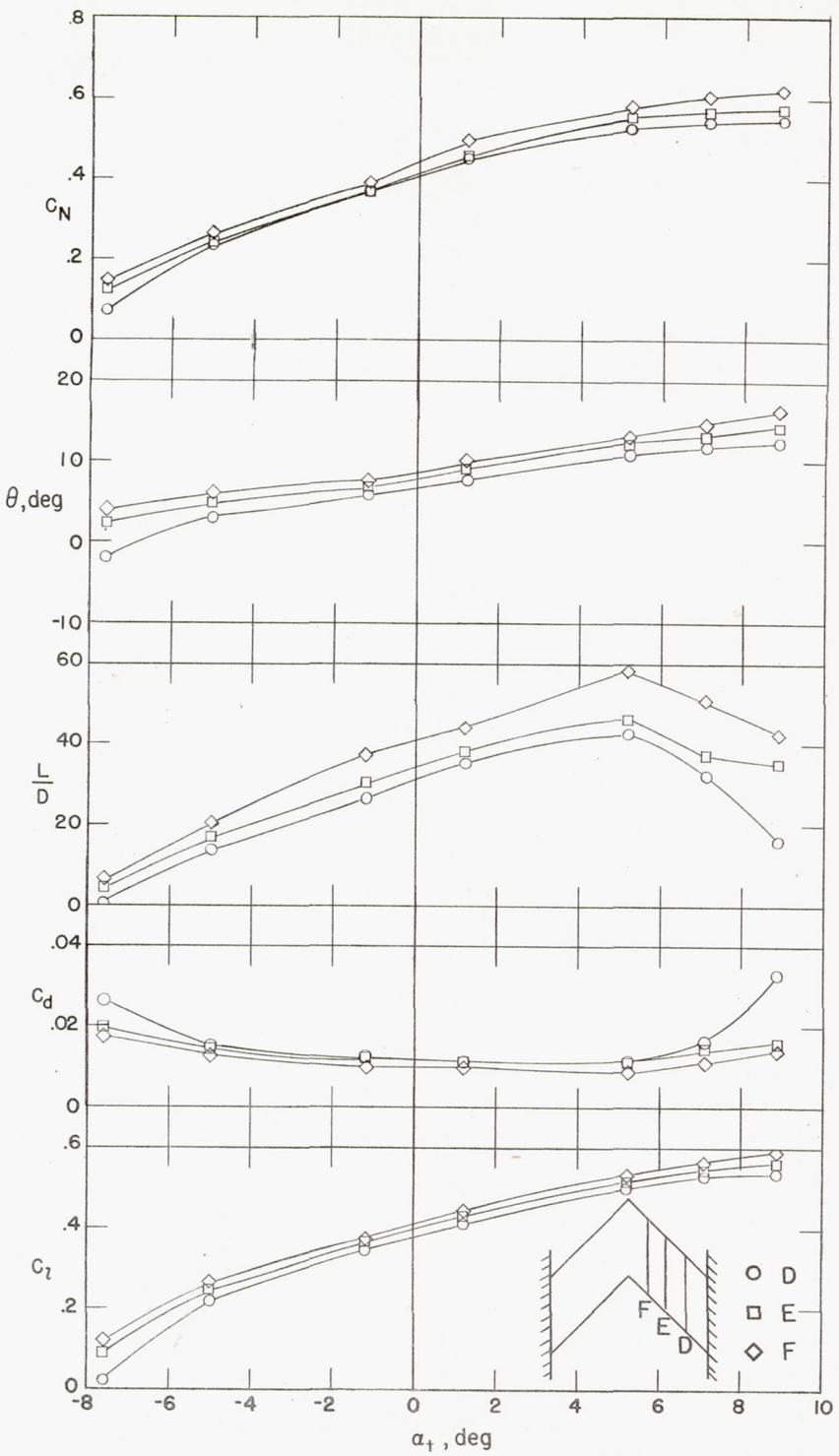

(g) Section characteristics.

Figure 13.- Concluded.

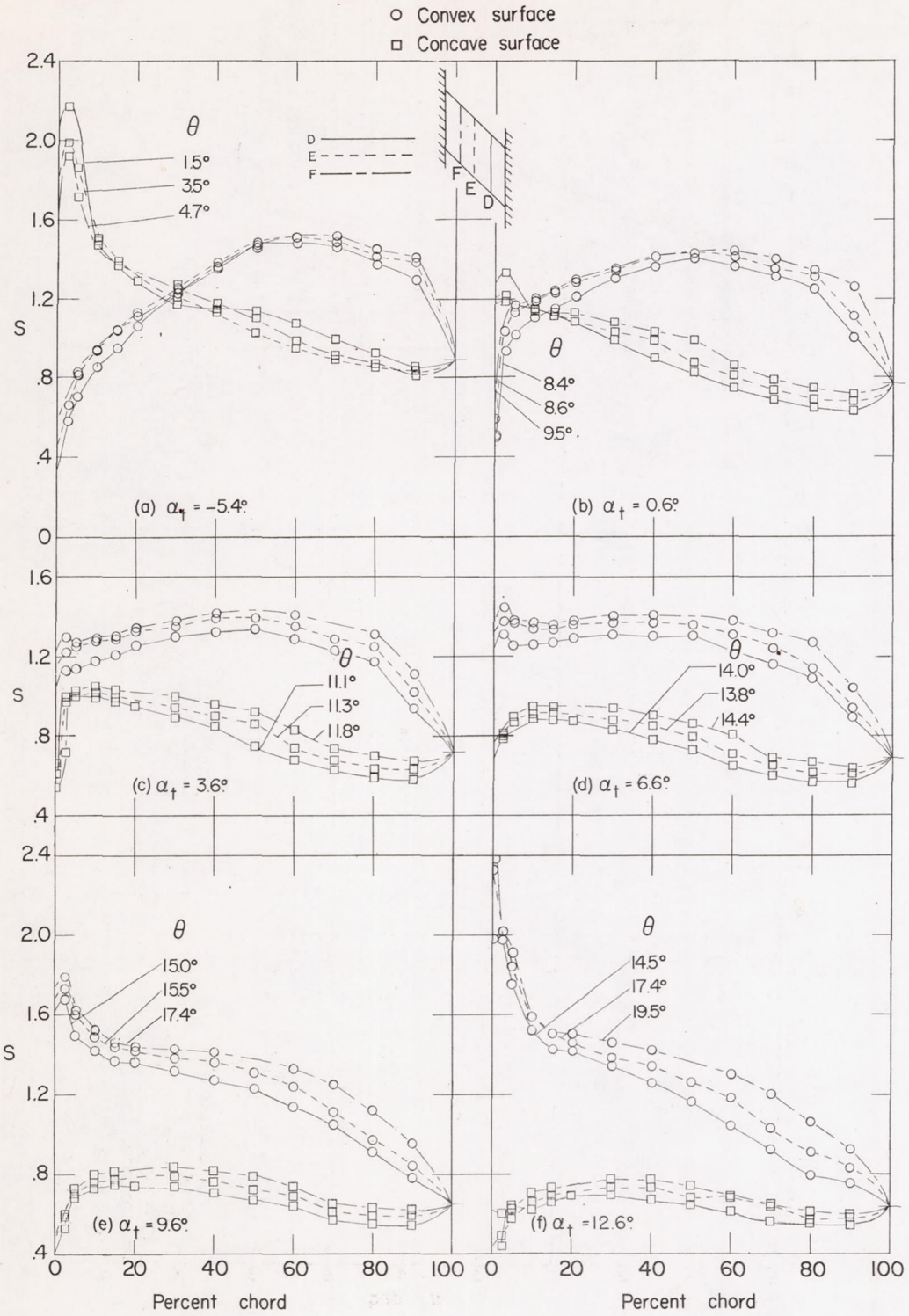

Figure 14.- Swept blade 2B blade surface pressure distributions and blade section characteristics for the cascade combination, $\beta = 45^{\circ}$ and $\sigma = 1.0$.

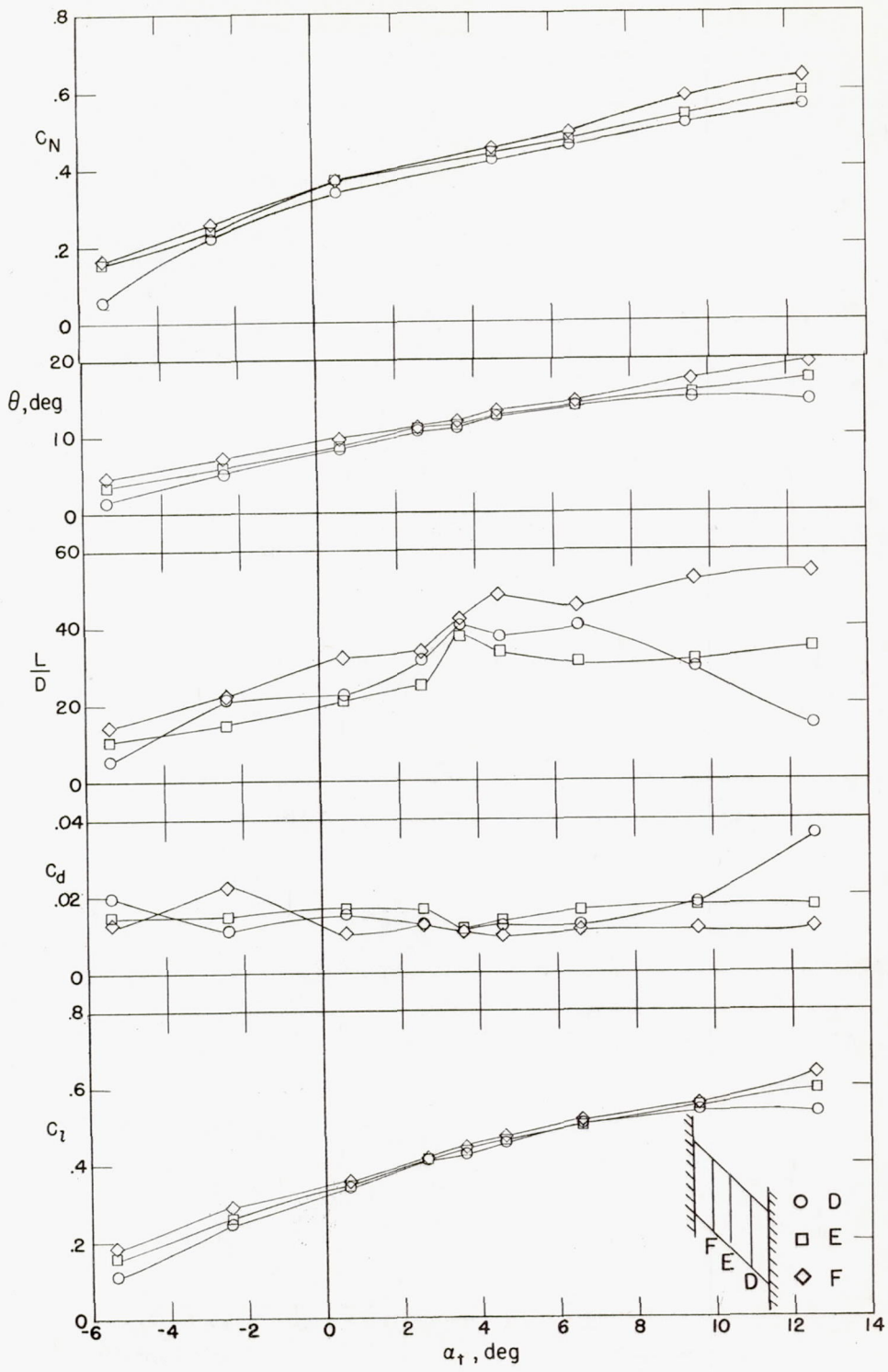

(g) Section characteristics.

Figure 14.- Concluded.

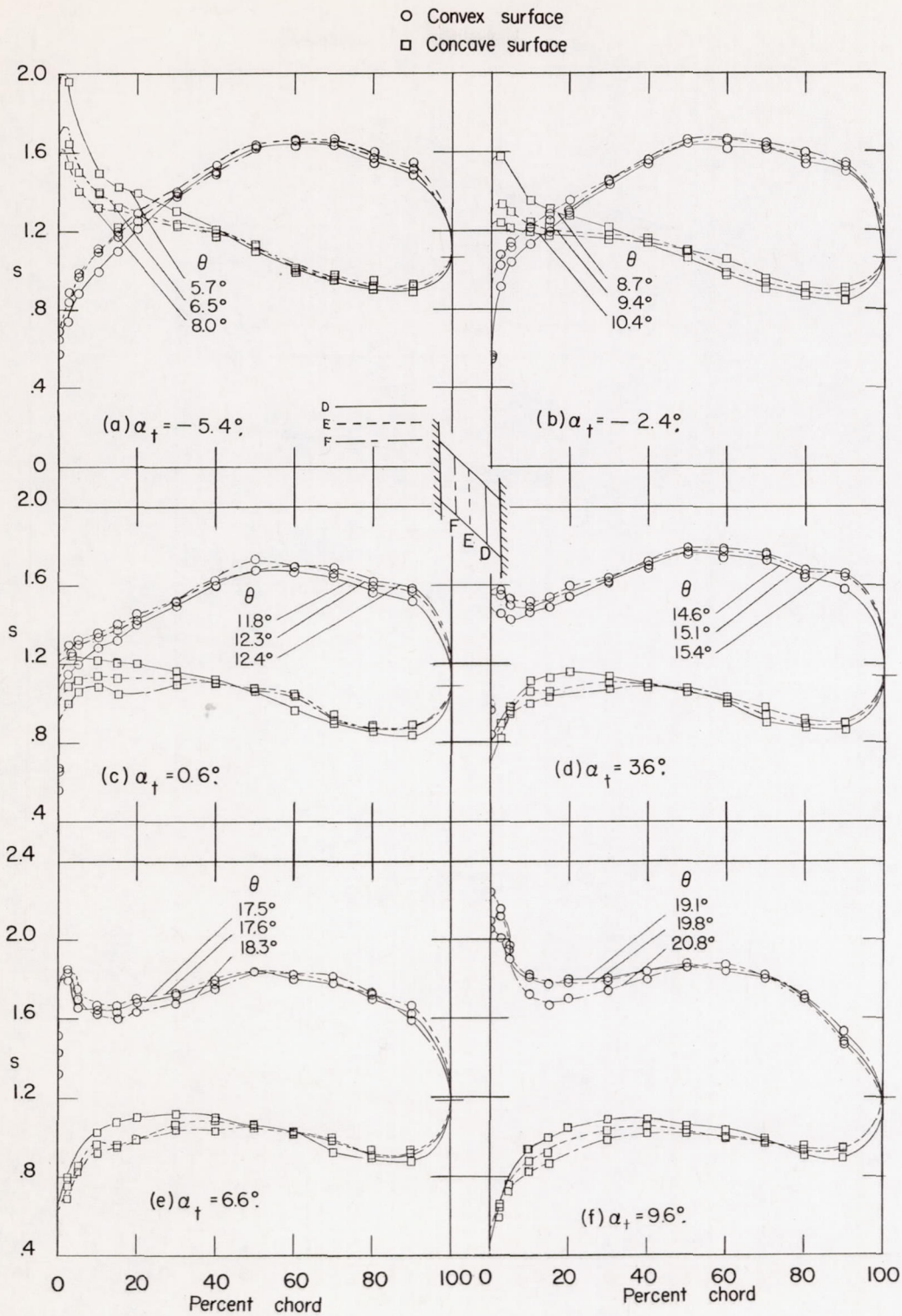

Figure 15.- Swept blade 2B blade surface pressure distributions and blade section characteristics for the cascade combination, $\beta = 0^{\circ}$ and $\sigma = 1.0$.

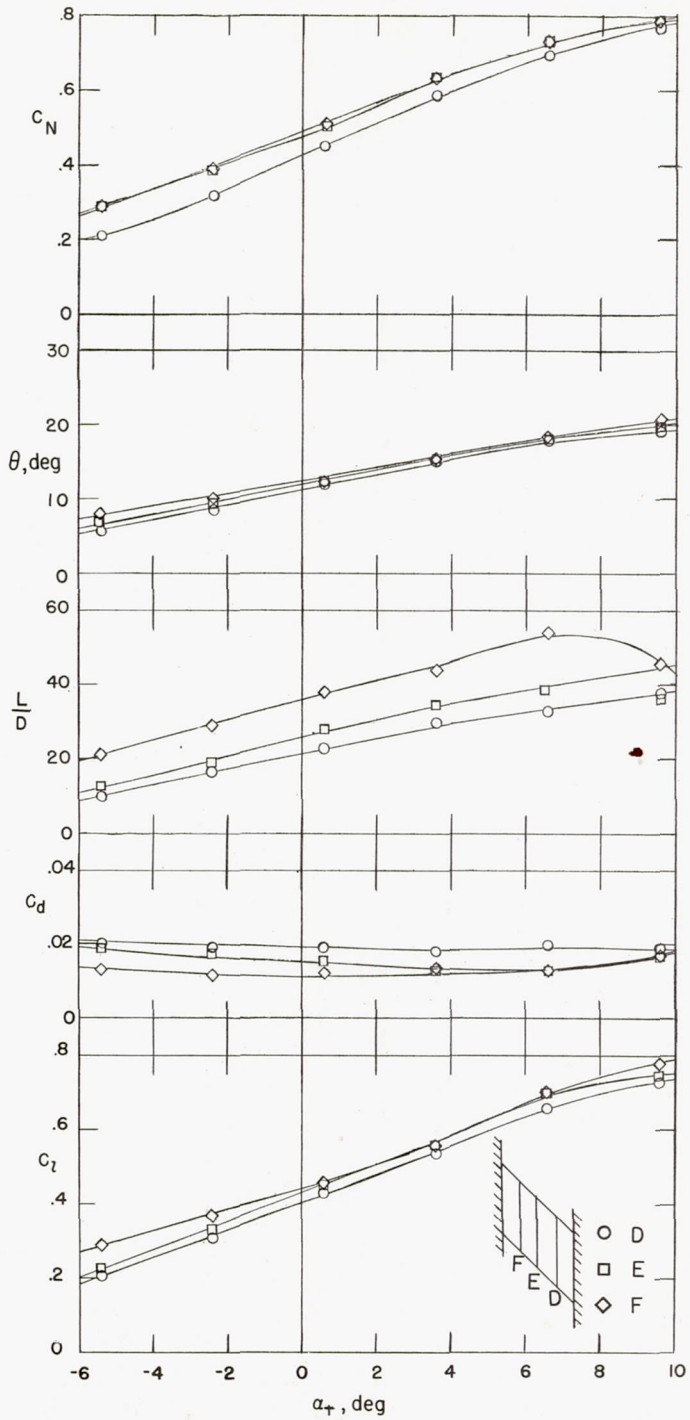

(g) Section characteristics.

Figure 15.- Concluded.

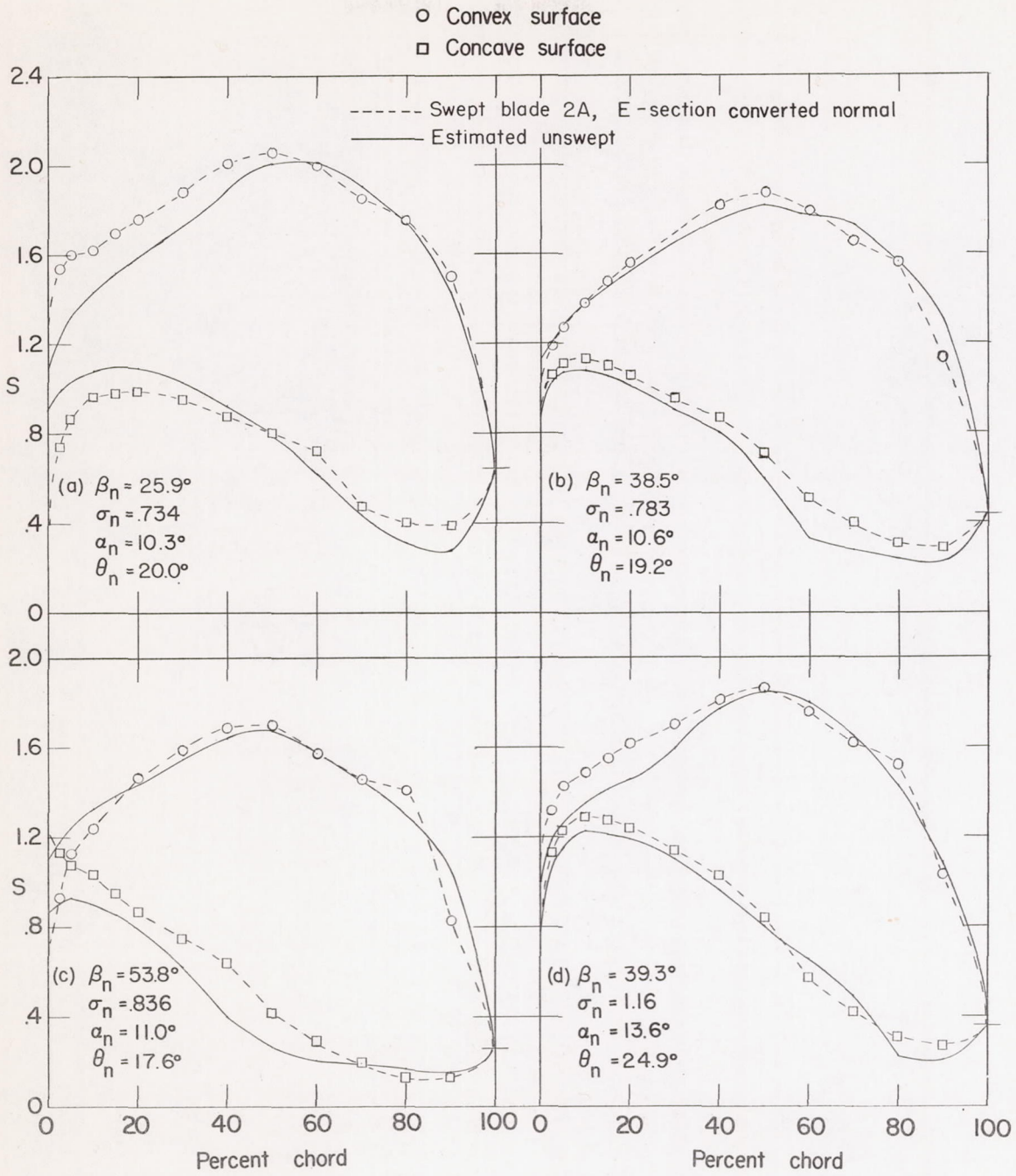

Figure 16.- Comparison of the converted-normal blade surface static pressure distributions of the E-section of swept blade 2A with the pressure distributions estimated for the unswept 65-(14.1A_2I8_b)14.1 blade section by the method of reference 4 for the same cascade parameters normal to the blade leading edge.

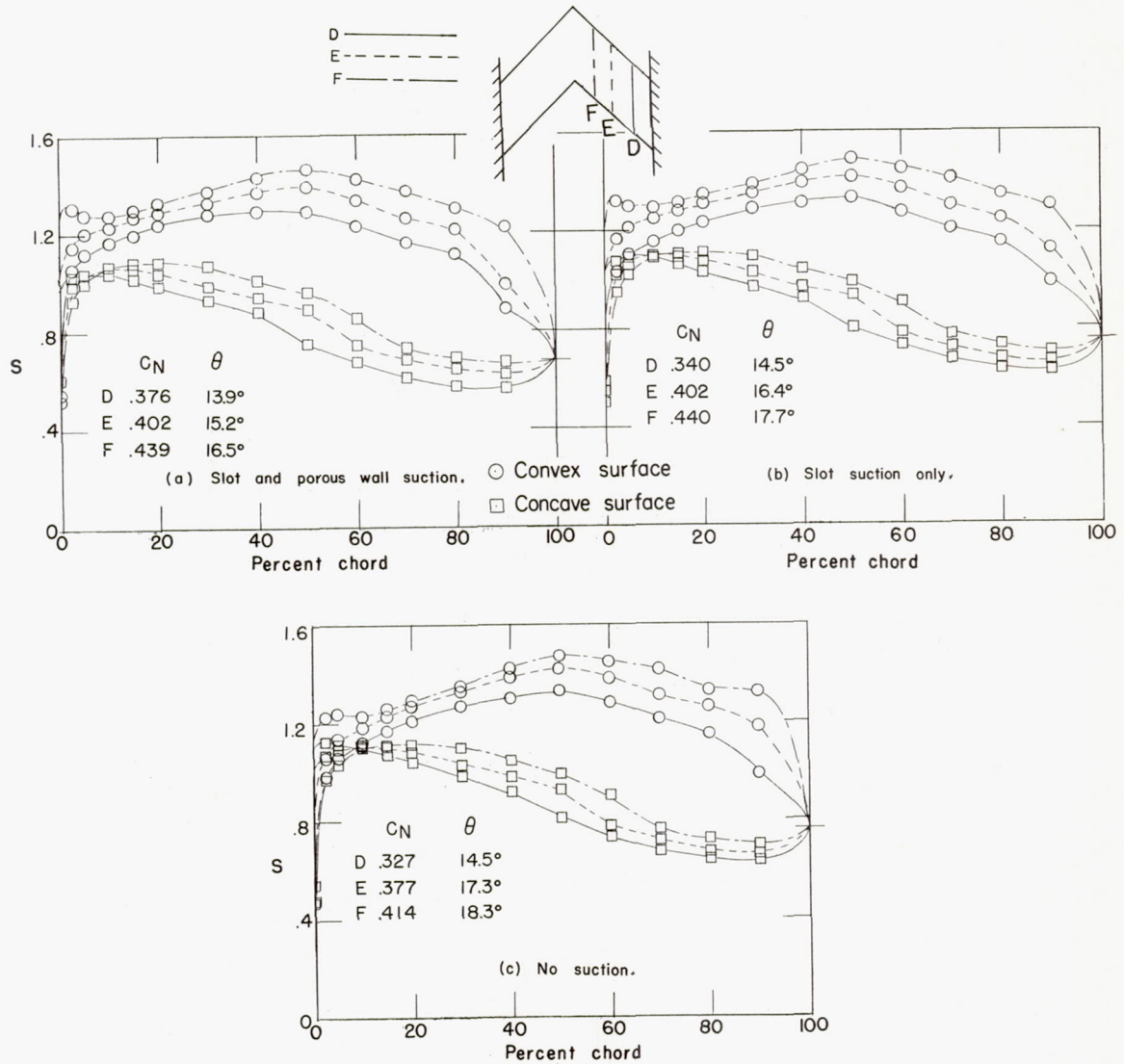

Figure 17.- Comparison of blade surface pressure distributions and section characteristics of swept blade 2A with suction conditions for the cascade combination, $\alpha_t = 2.8°$, $\beta = 45°$, and $\sigma = 1.25$.

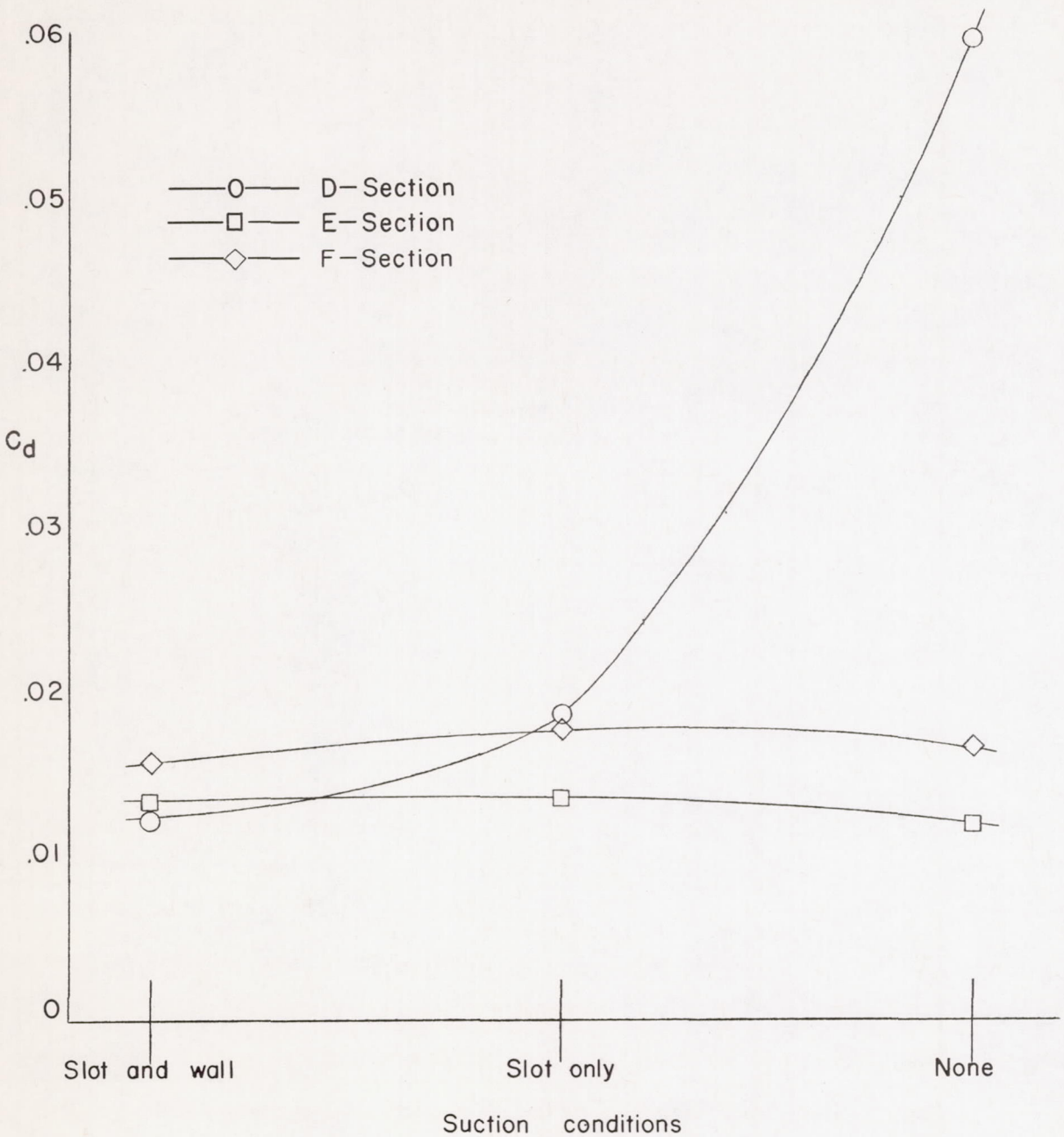

(d) Variation of drag coefficient with suction conditions for blade 2A at $\beta = 45^{\circ}$, $\sigma = 1.25$, and $\alpha_t = 2.8^{\circ}$.

Figure 17.- Concluded.

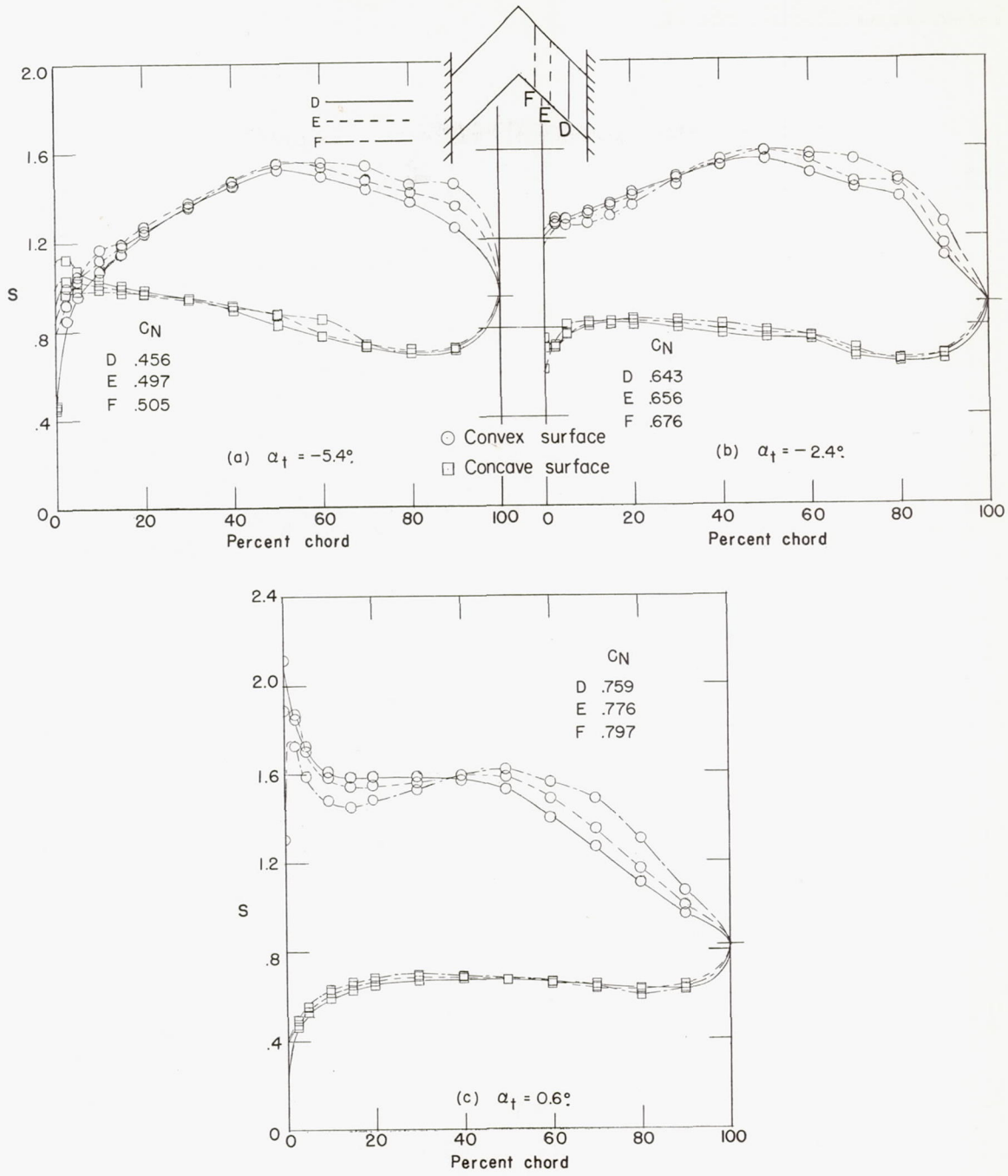

Figure 18.- Blade surface pressure distribution and blade section characteristics for the isolated case of swept blade 2A with no suction.

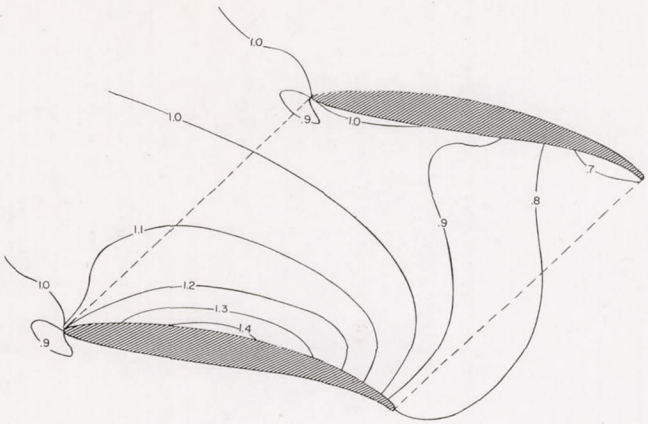

(a) F-section.

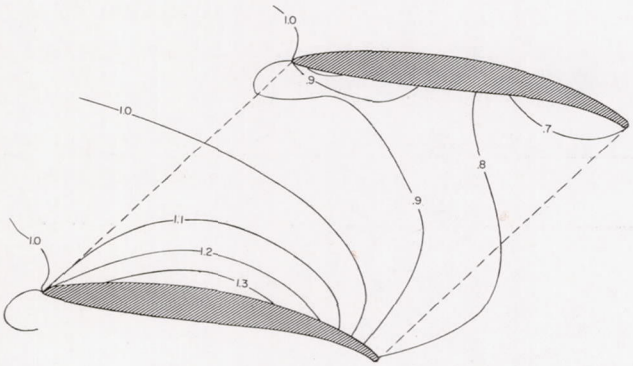

(b) E-section.

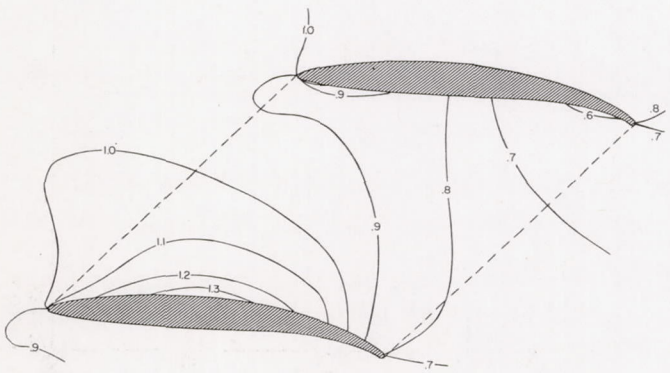

(c) D-section.

Figure 19.- Pressure coefficient contours through the blade passage at D, E, and F sections of blade 2B at a cascade combination of $\beta = 45^{\circ}$, $\sigma = 1.0$, and $\alpha_t = 3.6^{\circ}$.

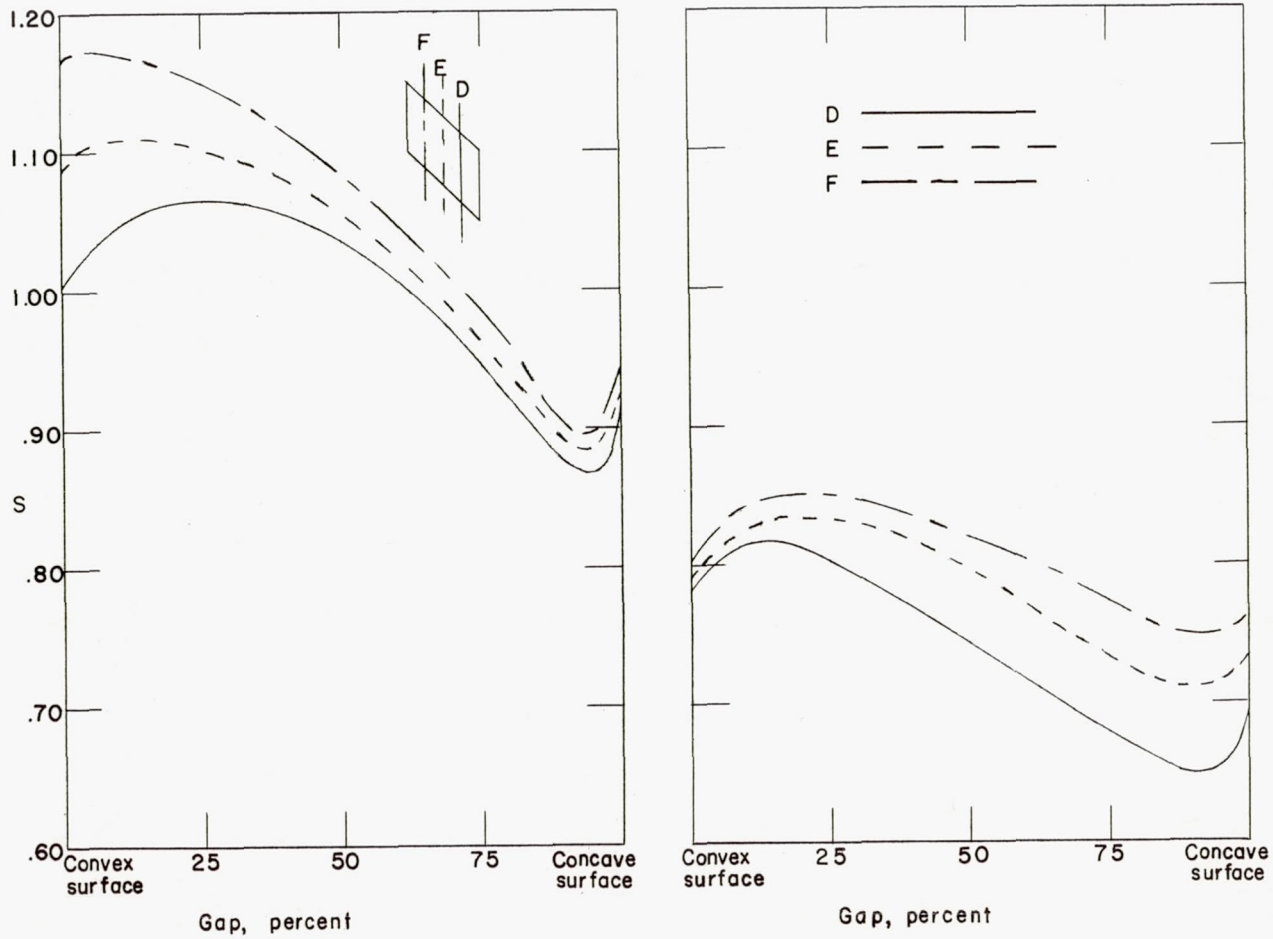

(a) Leading edge.

(b) Trailing edge.

Figure 20.- Static-pressure coefficient of blade 2B at $\beta = 45^{\circ}$, $\sigma = 1.0$, and $\alpha_t = 3.6^{\circ}$ plotted against passage gap at the leading- and trailing-edge lines.

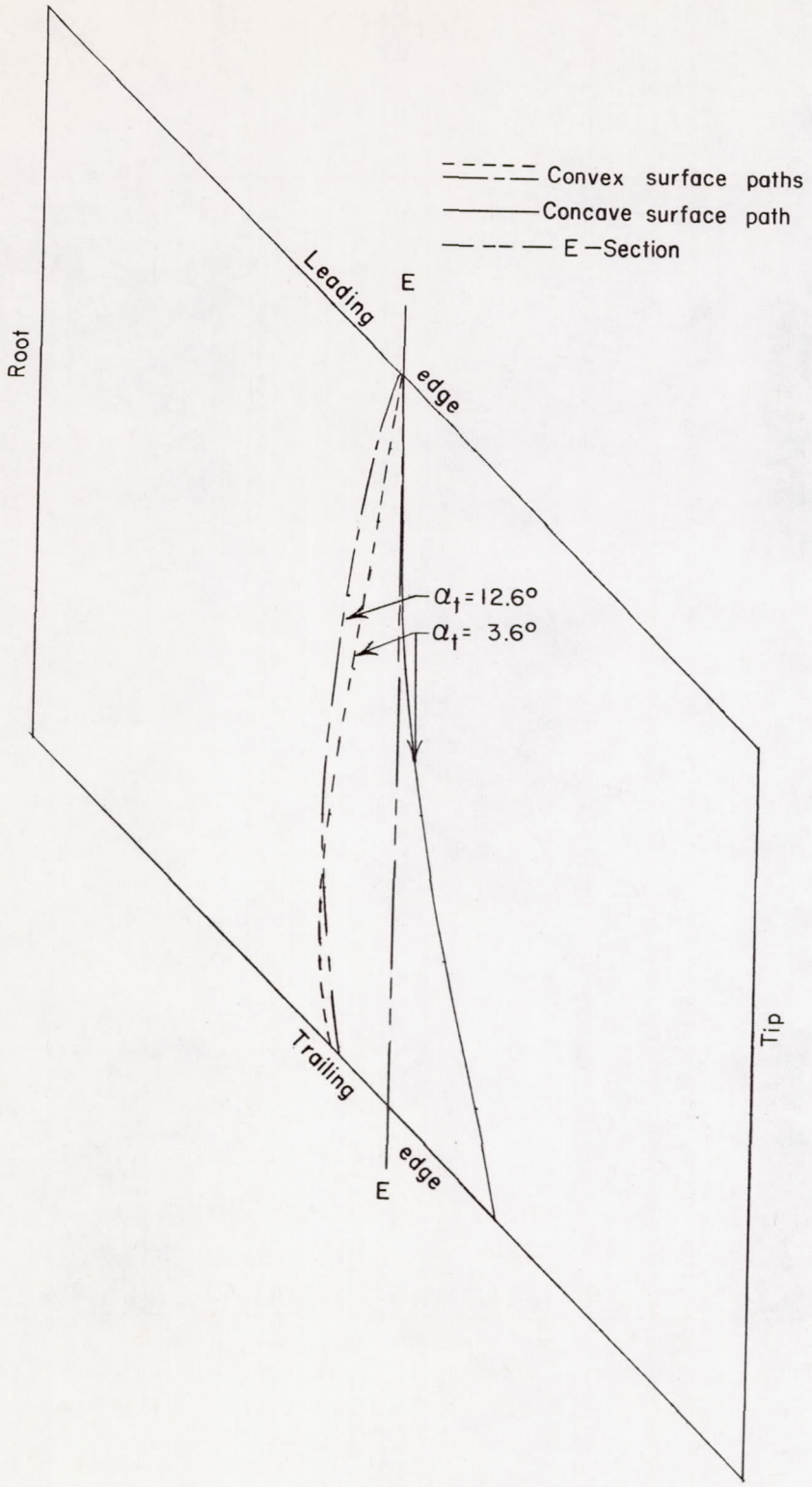

Figure 21.- Calculated streamline path at E-section of blade 2B at $\beta = 45°$, $\sigma = 1.0$, and $\alpha_t = 3.6°$ and $\alpha_t = 12.6°$.

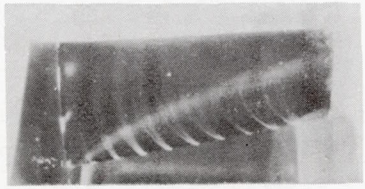

(a) $\alpha_t = -1.0^\circ$.

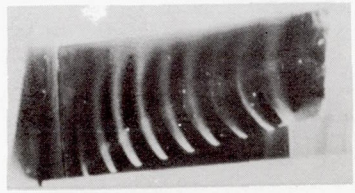

(b) $\alpha_t = 2.0^\circ$.

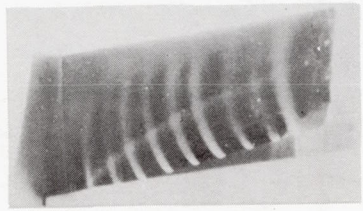

(c) $\alpha_t = 5.0^\circ$.

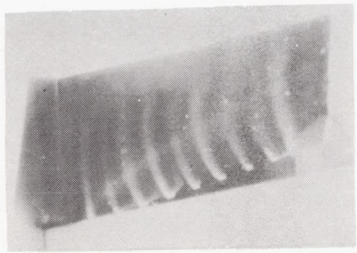

(d) $\alpha_t = 8.0^\circ$.

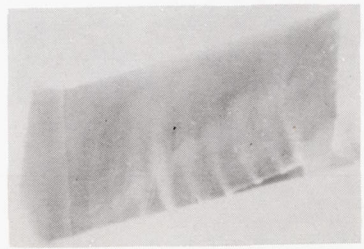

(e) $\alpha_t = 11.0^\circ$. L-82061

Figure 22.- Smoke traces over the convex surface of blade 2B at $\beta = 45^\circ$, $\sigma = 1.0$.

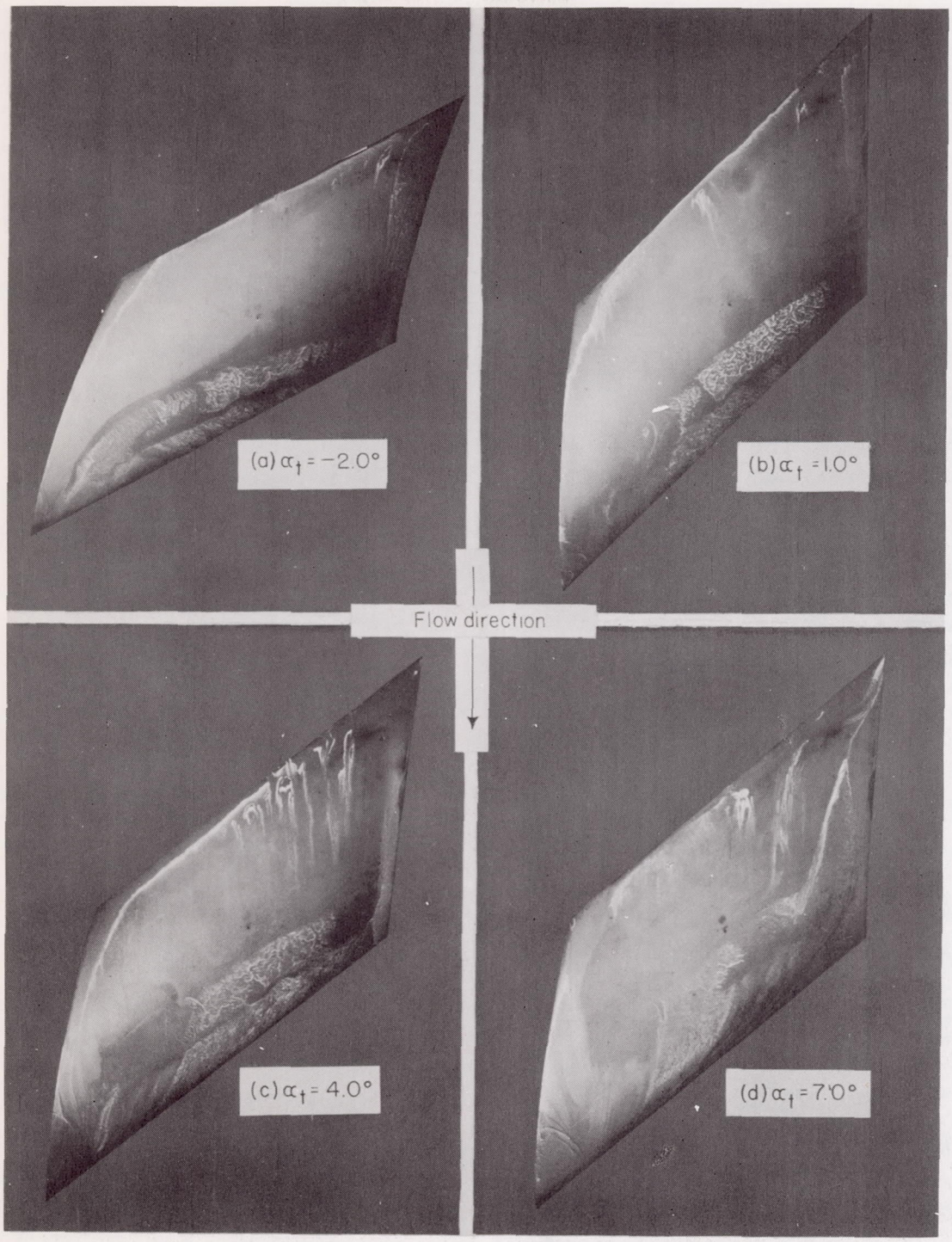

L-82062

Figure 23.- Results of tests on the convex surface of blade 2B at $\beta = 45°$ and $\sigma = 1.0$ over a range of angles of attack using fluorescent powder.

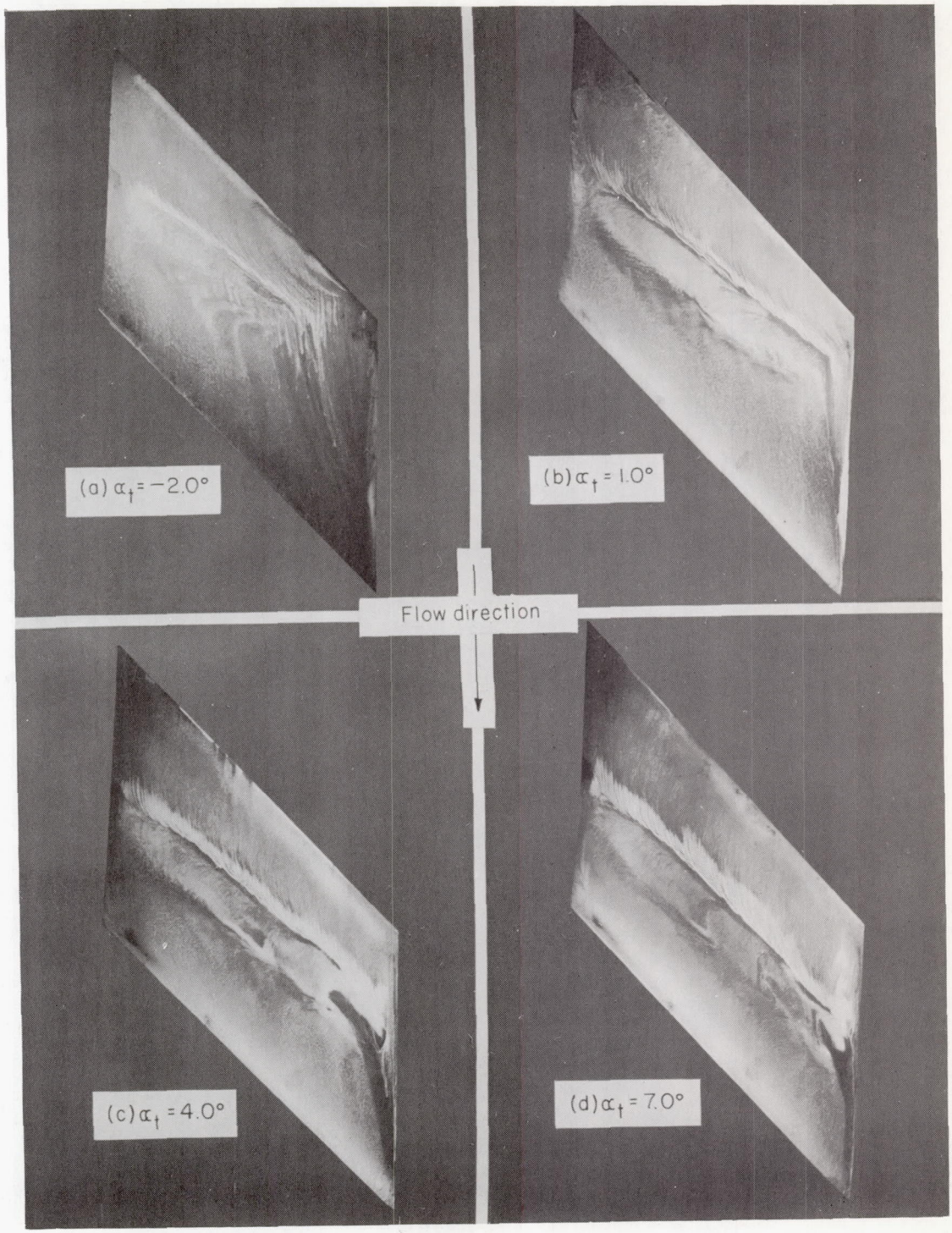

L-82063

Figure 24.- Results of tests on the concave surface of blade 2B at $\beta = 45°$ and $\sigma = 1.0$ over a range of angles of attack using fluorescent powder.

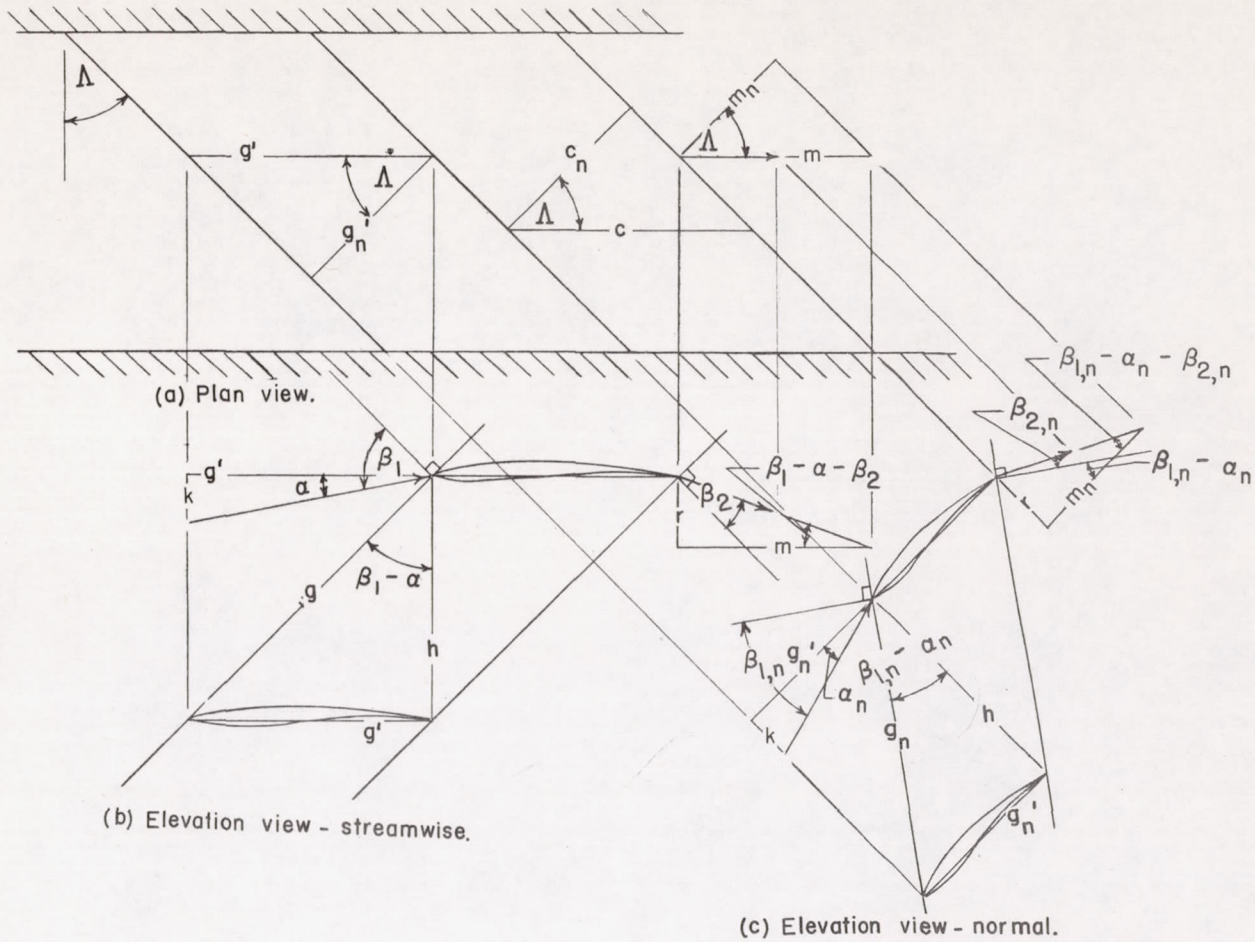

Figure 25.- A plan and two elevation views of a cascade of untwisted swept blades.